Old Dominion University

ODU Digital Commons

2023

Generation and Characterization of Magnetized Electron Beam From a DC High Voltage Photogun for Electron Beam Cooling Application

S.A.K. Wijethunga
Old Dominion University

M. A. Mamun

R. Suleiman

P. Adderley

B. Bullard

See next page for additional authors

Follow this and additional works at: https://digitalcommons.odu.edu/physics_fac_pubs

Part of the Engineering Physics Commons, and the Nuclear Commons

Authors

S.A.K. Wijethunga, M. A. Mamun, R. Suleiman, P. Adderley, B. Bullard, J. Benesch, Jean R. Delayen, J. Grames, C. Hernandez-Garcia, F. Hannon, Geoffrey A. Krafft, G. Palacios-Serrano, M. Poelker, M. Stefani, Y. Wang, and S. Zhang

Full Length Article

Generation and characterization of magnetized electron beam from a DC high voltage photogun for electron beam cooling application

S.A.K. Wijethunga [a,b,*], M.A. Mamun [b], R. Suleiman [b], P. Adderley [b], B. Bullard [b], J. Benesch [b], J.R. Delayen [a,b], J. Grames [b], C. Hernandez-Garcia [b], F. Hannon [b], G.A. Krafft [a,b], G. Palacios-Serrano [b], M. Poelker [b], M. Stefani [a], Y. Wang [b], S. Zhang [b]

[a] *Old Dominion University, Norfolk, VA 23529, USA*
[b] *Thomas Jefferson National Accelerator Facility, Newport News, VA 23606, USA*

ABSTRACT

One of the most challenging requirements for the proposed Electron–Ion Collider is the strong cooling of the proton beam, which is key to achieving the collider's desired luminosity of order 10^{33}–10^{34} cm^{-2} s^{-1}. Magnetized bunched-beam electron cooling could be a means to achieve the required high luminosity, where strong cooling is accomplished inside a cooling solenoid where the ions co-propagate with an electron beam generated from a source immersed in a magnetic field. To increase the cooling efficiency, a bunched electron beam with high bunch charge and high repetition rate is required. This work describes the production and characterization of magnetized electron beam using a compact 300 kV DC high voltage photogun and bi-alkali antimonide photocathode. Beam magnetization was studied using a diagnostic beamline that includes viewer screens for measuring the shearing angle of the electron beamlet passing through a narrow upstream slit. Simulations and corresponding measurements of beam magnetization are presented as a function of laser spot size and magnetic field strength. Correlated beam emittance with magnetic field (0–0.15 T) at the photocathode was measured for various laser spot sizes. Measurements of photocathode lifetime were carried out at different magnetized electron beam currents up to 28 mA, and bunch charge up to 0.7 nC (not simultaneously).

1. Introduction

The proposed high-energy, high-luminosity, polarized Electron–Ion Collider (EIC) is one of the highest priorities for future nuclear physics research [1]. One of the critical requirements of the proposed collider design is to obtain ultra-high luminosity, exceeding 10^{33} cm^{-2} s^{-1}, which is a few hundred times larger than the luminosity achieved at the Hadron–Electron Ring Accelerator (HERA) at DESY [2]. Key to achieving the EIC's desired luminosity is strong cooling of the ion beams to counteract emittance degradation induced by intra-beam scattering [3], maintain emittance during electron–ion collisions, and to extend the luminosity lifetime.

Cooling can be explained as a reduction of the six-dimensional (6D) phase space volume occupied by the beam (for the same number of particles), or equivalently, cooling is a reduction in the random motion of the beam. There are two main types of cooling mechanisms for ion beams, some demonstrated and some only proposed: conventional electron cooling (including DC beam cooling [4] and bunched beam cooling [5,6], both with and without magnetized beams [7,8]) and stochastic cooling (including microwave stochastic cooling

[9–12], optical stochastic cooling [13,14], and coherent electron cooling (CeC) which has several variants including free-electron laser [15], plasma-cascade or microbunched [16–18]).

The proposed EIC cooler design requires strong cooling of hadrons at energies up to 100 s of GeV and requiring less than one hour of cooling time. Due to the unfavorable $1/\gamma^{2.5}$ factor [19] in the cooling rate, it is a challenging task to achieve these requirements because traditional DC electron cooling, which has successfully cooled hadron beams below 10 GeV, is ineffective at the higher energies and conventional stochastic cooling is not fast enough for bunched beam cooling [20,21]. The successful development of different strong high energy proton cooling options such as CeC and magnetized electron cooling with bunched beams are needed to open a clear path to achieving high luminosity. All of the proposed strong-hadron cooling methods require very high-average-current unpolarized electron beams, at high bunch charge, and with low emittance. Implementation necessitates that the electron gun must exhibit a long lifetime.

G.I. Budker first proposed electron cooling in 1965 to increase the luminosity of hadron colliders [22]. The idea behind this is when an

electron beam with temperature T_e co-propagates with an ion beam with temperature T_i with $T_e < T_i$ and with the same average velocity, Coulomb collisions between ions and electrons lead to a transfer of thermal energy from ions to the electrons. Thermal equilibrium is reached when both particles have the same transverse kinetic energy. The electron cooling method was successfully tested in 1974 at NAP-M (Russian acronym for Antiproton Accumulator Model) with low-energy non-relativistic protons [23]. In 2005, Fermilab demonstrated relativistic electron cooling of 8.9 GeV/c antiprotons at its Recycler facility with a 4.3 MeV electron beam [4]. A collaboration between Jefferson Lab (USA) and Institute of Modern Physics (IMP, China) successfully demonstrated for the first-time cooling in both the longitudinal and transverse directions using a beam of electron bunches [5]. Brookhaven National Lab (BNL) recently demonstrated the world's first bunched-beam electron cooling of Au ions of energy 4.6 GeV/nucleon at its Low Energy Relativistic Heavy Ion Collider (RHIC) electron Cooler (LEReC) facility with electron beams of energies 1.6–2.6 MeV obtained via radio-frequency (RF) acceleration [6]. However, none of these experiments have met the extremely demanding conditions required by the EIC.

In 1977, Ya. S. Derbenev predicted that electron cooling efficiency could increase by up to two orders of magnitude if the process occurs inside a uniform longitudinal magnetic field, a process known as "magnetized electron cooling" [7,8]. The basic principle is as follows: when an electron beam travels through a long solenoid magnet through which the ion beam passes, the magnetic field forces the electrons to follow small helical trajectories thereby increasing the electron–ion interaction time while suppressing the electron–ion recombination, which is a severe problem, especially for heavy ions.

However, delivering the electron beam into the cooling solenoid poses a significant challenge. The radial fringe field at the entrance of the cooling solenoid exerts a large transverse momentum "kick" onto the electron beam making it impossible to obtain the desired electron trajectories inside the solenoid. However, as Ya. S. Derbenev proposed, the ill effects of the fringe field can be canceled if the electron beam is born in a similar solenoid magnetic field (aka magnetized beam) and passing through a fringe field at the exit of the photogun that produces a beam motion with equal transverse momentum but of opposite sign, such that the two fringe-field effects cancel [24]. Another way to explain this is to consider Busch's theorem [25], which states that the canonical angular momentum of a charged particle moving in an axially symmetric magnetic field is conserved. Therefore, to implement cooling inside a solenoid, the electron beam must be generated inside a magnetic field. To implement cooling at relatively high energy, the electron beam must be bunched and accelerated in a superconducting radio-frequency (SRF) linac, which might pose an additional challenge. The technique is shown schematically in Fig. 1.

Table 1 lists the magnetized electron beam specifications for Jefferson Lab's EIC (JLEIC) cooler design [26]. Although the JLEIC design was not adopted, magnetized cooling represents a compelling research topic and might be applicable over some range of operating conditions of the EIC design at Brookhaven National Lab (BNL). The maximum proton beam energy of the JLEIC design was 100 GeV, whereas the EIC requires 275 GeV proton beams. For the higher proton beam energies, the applicability of magnetized beams for cooling suffers limitations, both with technology and cost. To implement magnetized beam cooling for 275 GeV protons, very high solenoid fields and very long coolers are required. The number of Larmor periods within the solenoid must remain the same as the proton energy increases and eventually the solenoid becomes too long and too strong to afford. Though technically feasible, other cooling options might be preferable. Today's EIC baseline design depends on microbunched CeC [17,18].

Referring to Table 1, the reason for the loose requirement on the transverse normalized emittance is because cooling rates of a magnetized electron beam are ultimately determined by electron longitudinal energy spread rather than the transverse emittance. This is because the

Table 1
The magnetized electron beam requirements of JLEIC cooler.

Parameter	JLEIC requirements
Bunch charge [nC]	3.2
Average current [mA]	140 (at > 400 kV)
Repetition rate [MHz]	43.3
Transverse normalized emittance (uncorrelated) [mm mrad]	<19
Normalized drift emittance (correlated) [mm mrad]	36
Photocathode spot radius - flat top [mm]	2.2
Bunch length - flat top [ps]	60
Magnetic field at photocathode [T]	0.1

transverse motion of the electrons is significantly diminished by the strong longitudinal magnetic field. No further discussion of the energy spread will be presented here since the main contribution to energy spread comes from microbunching and space charge in the high energy circulator in the current cooler design for JLEIC [26]. Very high average current and bunch charge at relatively high bunch repetition rate are the noteworthy requirements that highlight the technical challenges of producing this beam. Delivering high average current and high bunch charge electron beam has been a topic of study at many accelerator facilities worldwide (some specific references are cited below).

When considering electron guns for the production of high average current and high bunch charge, there are different options to choose from, each with advantages and disadvantages: a normal conducting RF gun with a photocathode or rf-gridded thermionic emitter, an SRF gun with photocathode, and DC high-voltage guns with a photocathode or rf-gridded thermionic emitter.

In general, RF guns are used for high bunch charge applications, producing "stiff" MeV beams very quickly over a short distance. For many years, the world record for highest average current was the demonstration of the Boeing gun, with average current 32 mA [27] but thermal heat load management represents a significant challenge for normal conducting RF guns operating in CW mode [28].

The Fermilab Accelerator Science and Technology (FAST) facility [29] has successfully demonstrated the production of a magnetized electron beam using a normal conducting RF photogun in pulsed mode and at very low average current (<7.5 μA), with a solenoid magnet providing a strong longitudinal magnetic field at the photocathode [30, 31]. Recently, FAST demonstrated the generation of magnetized electron beams with 3 ps electron bunches at high bunch charge, 1.6 and 3.2 nC [32].

SRF guns promise CW operation with high average current and producing beam at MeV energy, but so far, only 0.15 mA average current has been demonstrated [33]. However, even if SRF guns could provide high average current, this technology might not be viable for magnetized beam applications because the Meissner effect [34] would oppose the application of the magnetic field at the photocathode from outside the SRF cavity. However, applying a magnetic field from inside the SRF cavity could be considered.

A DC high-voltage electron gun with rf-gridded emitter is a viable option, with many examples in operation or under development [35–37]. These types of electron guns can operate at modest vacuum levels and promise high reliability at high average current, but typically emit long electron bunches resulting in comparatively large energy spread. DC high voltage photoguns represent another viable option, providing great flexibility over bunch charge, repetition rates, and bunch length and in recent demonstrations (described below) have provided very high average current and approaching the ~100 mA specification for EIC cooling applications. Ion back bombardment of the photocathode [38] can limit the operating lifetime of the DC high voltage photogun, but there is wide ranging acceptance that alkali-antimonide photocathodes can be made impervious to ion bombardment. Both of these electron gun options were developed at Jefferson Lab for the JLEIC magnetized-beam cooler. The DC high voltage gun with rf-gridded thermionic gun operating at 90 kV bias voltage has so
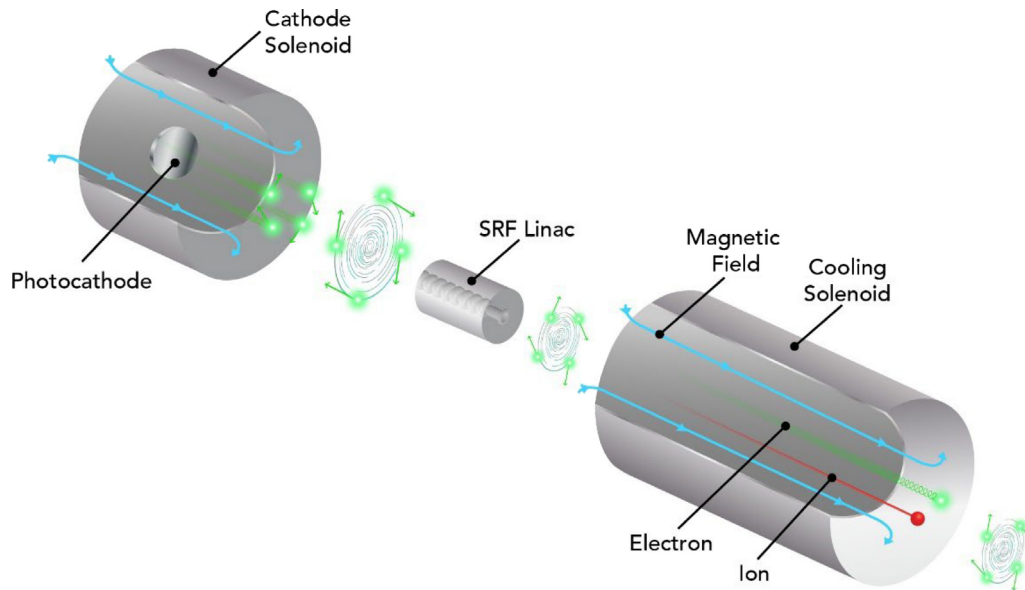
Fig. 1. Illustration of magnetized cooling: generation of magnetized beam inside the cathode solenoid, beam acceleration, and inside the cooling solenoid where the electron and ion co-propagate together at the same average velocity.

far demonstrated magnetized beam at average current 20 mA with electron bunch length of the order 300 ps and is described in Ref. [37]. The production of magnetized electron beam using a DC high voltage photogun is the focus of this paper.

Recent work at Jefferson Lab and Cornell University [39] has shown that DC high-voltage photoguns followed by superconducting accelerating cavities produce beams as good or better than RF guns with similar parameters. The DC gun used for the Jefferson Lab's Free-Electron Laser reliably provided 135 pC bunches at an average current of up to 9 mA for many years [40]. Cornell University holds the world record for high average current (65 mA) and very short nC bunch charges, but not simultaneously [39]. BNL has also has made significant progress generating 30 mA electron beams for the LEReC program [41].

We generated magnetized electron beam (i.e., beam dominated by canonical-angular-momentum (CAM)) using a 300 kV DC high-voltage photogun employing an inverted insulator geometry and bi-alkali antimonide (K_2CsSb) photocathode. Initially the work supported JLEIC which was not adopted, but the work remains relevant today in support of the broader EIC effort. Characterization of the magnetized beam was done by measuring the beam size and rotation angle variation as a function of the magnetic field at photocathode, with measurements compared to simulation predictions from General Particle Tracer (GPT) [42]. We studied the transverse emittance associated with the magnetized beam by measuring and simulating the emittance for different magnetic fields at photocathode and for various laser spot sizes. High current magnetized electron beams were produced to study the photocathode lifetime. We also investigated the space charge effect in low energy magnetized beams as a function of magnetic field strength, gun high-voltage, laser pulse width, and spot size with measurements compared to simulations.

2. Magnetized electron source

The prototype magnetized electron source is located at the Gun Test Stand (GTS) inside the Low Energy Recirculator Facility (LERF) building at Jefferson Lab. Key subsystems include the bi-alkali antimonide photocathode preparation chamber, the DC high-voltage photogun, two different drive laser systems, cathode solenoid used to magnetize the beam, and diagnostic beamline. Some of these systems are shown in Fig. 2: descriptions follow.

2.1. Photocathode preparation chamber

The electron cooler application requires a stable and reliable high average current magnetized electron beam. As such, alkali-antimonide photocathodes were chosen because the material provides high quantum efficiency (QE), fast response-time and robustness at high average current. A load-locked bi-alkali antimonide Cs_xK_ySb photocathode preparation chamber was built and installed behind the gun high-voltage chamber [43]. Two different substrates, GaAs and Mo were used to fabricate the photocathodes. GaAs was initially used since it was readily available and the Mo substrate was used for high current beam delivery, as it has superior thermal conductivity, which helps avoid QE degradation due to associated alkali loss by laser-induced heating [44]. Photocathodes were fabricated using a two-step sequential deposition technique [45]. The first thin Sb film was deposited from a heated crucible. The thickness was varied by choosing different deposition times. Then Cs and K were deposited using an effusion source containing both species [43]. A stainless-steel mask with 1, 3, and 5 mm diameter holes was used to limit the active area of the photocathode. Alkali deposition was discontinued when the photoemission current reached a maximum, providing QE of 5% or higher [45]. The chamber also consists of four magnetically coupled sample manipulators of different sizes. The main long manipulator was used to move pucks in and out of the gun chamber. Two short manipulators were used to move pucks to and from the heater and transfer the pucks to the long manipulator. The other short manipulator was used to store the pucks. Non-evaporable getter (NEG) and ion pumps maintained the vacuum in the 10^{-11} Torr range, and an RGA mass spectrometer (SRS model RGA200) was used to monitor the vacuum gas composition continuously during photocathode fabrication [43].

2.2. High-voltage dc photogun

A load-locked compact DC high-voltage photogun with inverted insulator geometry and spherical cathode electrode operating at or below 300 kV was built and installed for the study. The inverted-insulator design helps to minimize field emission because it reduces the total metallic area biased at high voltage. A specially designed screening electrode was attached to the cathode electrode to maintain the electric field less than 1 MV/m at the triple-point junction [46,47]. The maximum electric field strength inside the photogun is <10 MV/m.
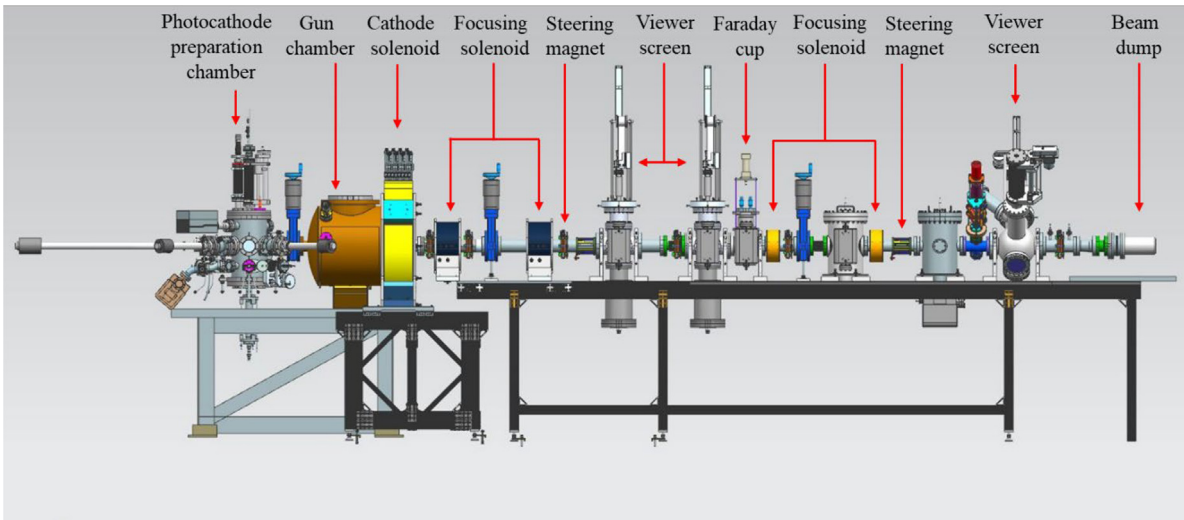
Fig. 2. The magnetized electron source and diagnostic beamline.

However, the asymmetric photogun design with the inverted insulator geometry and screening electrode creates an asymmetric electric field in the anode–cathode gap, deflecting the beam at the exit of the gun and making it difficult to center in a nearby downstream solenoid [48]. Because of this, it was important to use 3D field maps of the cathode–anode gap in simulations.

The anode, with an aperture diameter of 2 cm, located 9.0 cm from the photocathode was electrically isolated from ground potential to enable measurement of field emission from the cathode electrode and to enable biasing to repel downstream ions created by the beam. The drive laser beam passed through entrance and exit holes in the anode electrode with light delivered to the photocathode at 25° angle of incidence. A cylindrical focusing lens was used to adjust the laser beam spatial profile to account for the incident angle. Two different high-voltage power supplies were used at the GTS to energize the photogun: a 500 kV, 5 mA Cockcroft–Walton SF_6 gas-insulated DC high-voltage power supply and a Spellman high-voltage power supply with 225 kV biased voltage and 30 mA average current with a power limit of 3 kW. The photogun was high voltage conditioned to 360 kV using krypton gas to eliminate field emitters. After high-voltage (HV) conditioning the gun with cathode solenoid off, we found that powering the solenoid can trigger field emission when gun is biased at nominal HV. The gun was re-conditioned with solenoid currents up to 400 A (0.15 T at the photocathode) in steps of 25 A. To ensure cathode solenoid does not trigger new field emission, we avoided turning on the solenoid when the gun is biased at nominal HV by first lowering the gun HV to 100 kV. The vacuum pressure inside the photogun while delivering electron beam was about 1×10^{-11} Torr achieved using NEG sheet and ion pumps [46].

2.3. Drive lasers

Two different drive lasers were used throughout this project: one for high average current generation and one for high bunch charge delivery [49]. For high current generation, a master-oscillator-power-amplifier system, composed of a 1066 nm gain-switched diode laser and multistage Yb-fiber amplifier chain followed by a harmonic converter, was constructed [50]. It provided Watts of power with picosecond light pulses at 533 nm, adjustable pulse repetition rates from 10 s of MHz to a few GHz, variable pulse width from 10 s to 100 s of picoseconds full-width at half-maximum (FWHM), and direct synchronization to an external RF signal without requiring laser cavity length feedback or rf-laser phase locking systems. The second laser was a commercial ultrafast laser with pulse duration ∼1 ps (FWHM), 20 μJ pulse energy,

operating at 50 kHz pulse repetition and 1030 nm wavelength (NKT Origami). The infrared beam was converted to 515 nm using a BBO crystal. To meet the pulse length requirement, a pulse stretcher consisting of two diffraction gratings and reflectors arranged in a double pass configuration was built. The sub-picosecond pulses were lengthened to values between 75–120 ps (FWHM) by changing the dispersion length of the stretcher. An image-relaying optical transport was shared by both lasers to deliver the light beams from the drive laser enclosure to an optical diagnostic hutch before reaching the photogun chamber. The average power and laser pulse energy were continuously varied using a rotating waveplate attenuator. A low duty factor, machine-safe electron beam was produced using a rubidium titanyl phosphate Pockels cell and a mechanical shutter to protect the beamline yttrium aluminum garnet (YAG) viewer screens [43,49].

The transverse profile and size of the laser spot on the photocathode were measured and monitored by placing a beam splitter between the last lens and the viewport in the photogun high-voltage vacuum chamber. The diverted laser beam was guided to a charge-coupled device (CCD) camera positioned equidistant from the beam splitter and the photocathode. The image from the CCD camera was processed by Spiricon laser beam profiler software [49,51].

2.4. Cathode solenoid magnet

To magnetize the electrons, a solenoid magnet was positioned at the front of the gun chamber, 21.0 cm away from the photocathode. The solenoid has an inner diameter of 30.0 cm, outer diameter of 70.0 cm, and length 15.75 cm comprised of 16 layers of 20 turn water-cooled copper conductor with a cross section area of 0.53 cm^2 and total conductor length of 500 m. The conductor has 0.18 Ω resistance at 65 °C average temperature. The solenoid was energized with a magnet power supply (400 A, 80 V) to produce magnetic fields up to 0.15 T at the photocathode. The option of adding a yoke to the cathode solenoid magnet was studied but found to be impractical, as much for cost as magnetic and mechanical reasons. Fig. 3 shows a photograph of the cathode solenoid.

2.5. Diagnostic beamline

The beamline extends 4.6 m from the gun photocathode with YAG viewer screens located at 1.5, 2.0 and 3.75 m. The first two YAG viewer screen actuators also include slits (50 μm in y), used to create narrow "beamlets" oriented in the horizontal plane to enable measurement of beam rotation angles. Fig. 4 shows the YAG viewer screen, slit,
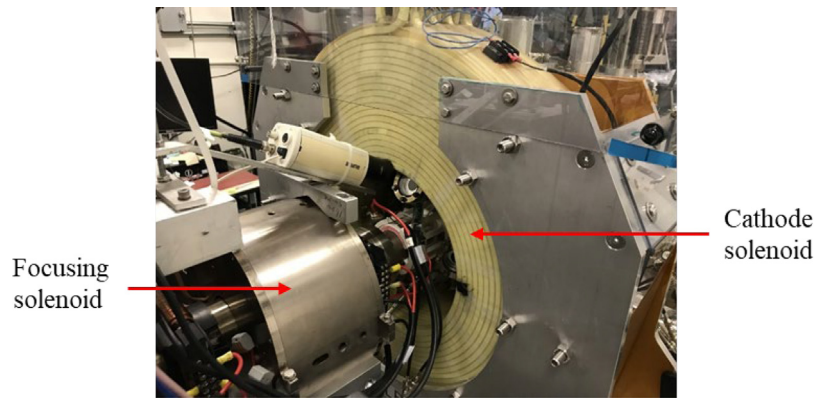
Fig. 3. The solenoid used to provide a longitudinal magnetic field at the photocathode, to magnetize the electron beam. Also shown is the first beamline focusing solenoid.
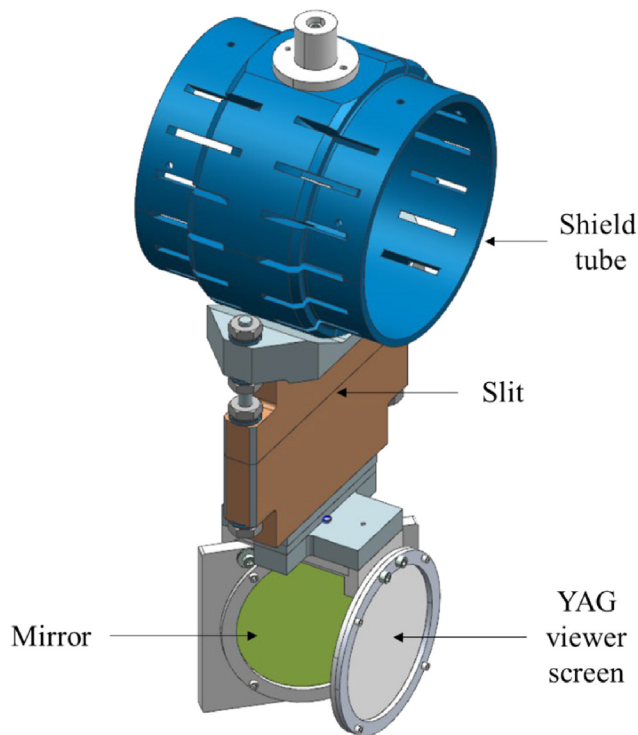

Fig. 4. The YAG viewer screen, slit, and shield tube combination.

Fig. 5. Longitudinal electric field of the photogun at 350 kV.

and shield tube combination. The beamline also contains four focusing solenoids, nine steering magnets, two ion collectors, two differential pumps, five ion pumps, two NEG pumps, a wire scanner, a Faraday cup, and a beam dump. The beamline diameter varied between 5 and 7 cm.

3. Modeling and simulations

CST Studio Suite's electromagnetic field solver [52] was used to create 3D electrostatic field map of the photogun with the maps extending from the photocathode surface to 0.14 m downstream (see Fig. 5). Opera [53] was used to provide 2D magnetic field map of the magnetizing solenoid which extend from the photocathode surface to the end of the beamline, including the entire beam pipe radius (see Fig. 6). Notice how the steel covers of the first two beamline solenoids distort the magnetic field of the magnetizing solenoid. These field maps were then used for particle tracking simulations in GPT program, with post-processing of results performed using MATLAB [54].
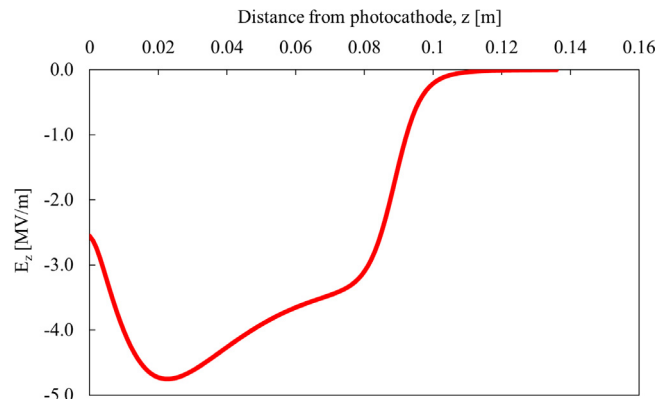
Since real life laser beams do not always possess Gaussian or flat top profiles, a grayscale bitmap image of the actual laser profile was used to create the initial electron distribution of the beam at the photocathode. Similarly, the photocathode QE was not always uniform across the photocathode active area. QE maps were obtained by scanning a low power laser across the photocathode while monitoring the emitted electron beam current. The initial beam distribution at the photocathode represents the actual laser spatial profile weighted by the QE profile sampled by the drive laser as shown in Fig. 7. This was a necessary step to see agreement between simulation and measurement.

To center the beam in the vacuum pipe, steering magnets were used in the GPT simulation, with settings optimized for each cathode magnetic field using the "GDFMGO" program [42], a multi-objective genetic global optimizer. The three YAG viewer screens were included in the simulation as well as the actual beampipe diameter. As a result, the GPT simulation tracks beam loss along the beamline.

4. Characterization of the magnetized electron beam

Two types of electron beams are shown in Fig. 8: a non-magnetized electron beam (left) with the electrons simply diverging, and a magnetized electron beam (right) generated inside a uniform longitudinal magnetic field, with electrons acquiring angular momentum at the exit of the magnetic field. The motion of a magnetized beam can be explained by the principle of conservation of canonical angular momentum, $\mathcal{L}$. Because canonical angular momentum is conserved, charged particle beams generated inside a solenoid field acquire a mechanical angular momentum outside of the magnetic field. Busch's theorem [25] explains the relationship between acquired orbital angular momentum, the applied magnetic field strength and the beam size at the photocathode.
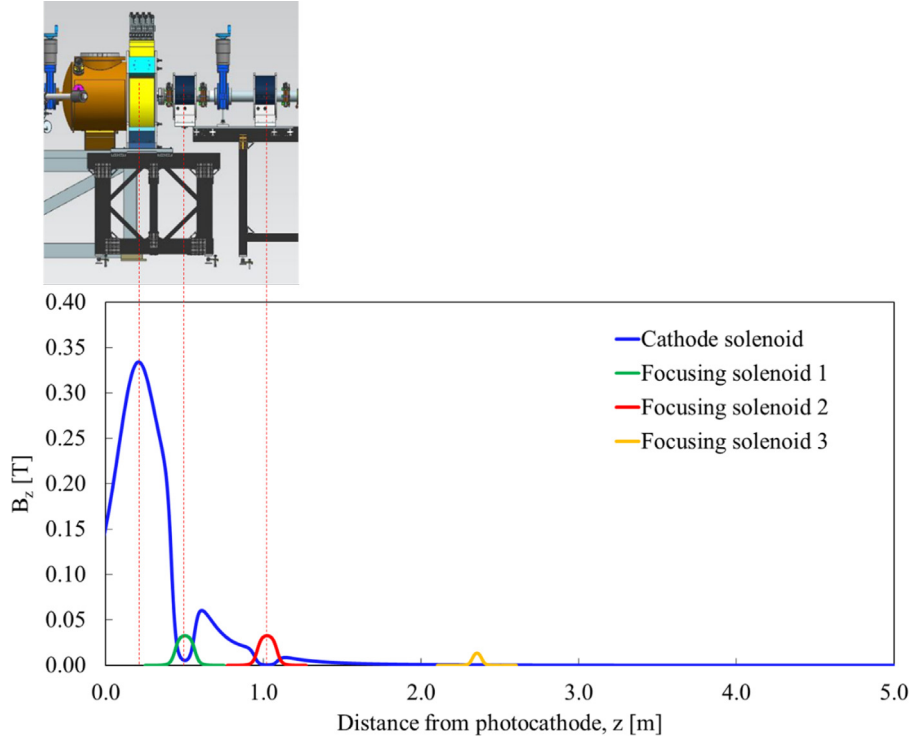
Fig. 6. Cathode solenoid field map at 400 A and the field maps of the three beamline solenoids.

For a cylindrically symmetric system, the canonical angular momentum of an electron in cylindrical coordinates is given by,

$$\mathcal{L} = \gamma m r^2 \dot{\phi} + \frac{1}{2} e B_z(z) r^2 = constant, \qquad (1)$$

where, $B_z(z)$ is the longitudinal magnetic field, γ is the Lorentz factor, $\dot{\phi}$ is the time derivative of the azimuthal angle ϕ, and m and e are the electron rest mass and charge, respectively. The average canonical angular momentum $\langle \mathcal{L} \rangle$ can be calculated by averaging Eq. (1) over the beam distribution. At the photocathode $\langle \dot{\phi} \rangle = 0$. Thus,

$$\langle \mathcal{L} \rangle = \frac{1}{2} e B_0 \langle r^2 \rangle = e B_0 r_0^2, \qquad (2)$$

where $B_0 = B_z(z=0)$ is the longitudinal magnetic field at the photocathode, and r_0 is the transverse root-mean-square (rms) beam size at the photocathode (for a Gaussian beam, $\langle r^2 \rangle = 2r_0^2$). Outside the magnetic field region $B_z = 0$ and the second term of the Eq. (1) vanishes. Thus,

$$\langle \mathcal{L} \rangle = \gamma m \langle r^2 \rangle \dot{\phi}, \qquad (3)$$

producing a mechanical angular momentum. The average angular velocity in this region is given by,

$$\dot{\phi} = \omega_L = \frac{e B_0}{2 \gamma m}, \qquad (4)$$

which is also known as the Larmor frequency. In the sections below, we characterize the magnetized beam in terms of electron beam size, beam rotation angle, and correlated/drift emittance, as a function of the applied magnetic field at the photocathode.

4.1. Beam size variation with the magnetic field at the photocathode

Magnetized beam was generated from the photogun and delivered to the beam dump at the end of the diagnostic beamline. In the laboratory and in simulation, beam size measurements were made along the length of the diagnostic beamline using the three YAG viewer screens, for magnetic fields at the photocathode ranging from 0 to 0.15 T obtained by changing the cathode solenoid current from 0 to 400

A. For the tests described in this section, the beamline solenoids were not powered: only the magnetizing solenoid affected beam size at the YAG viewer screens. For simplicity, we are presenting the rms beam size calculated as $\sigma = \sqrt{\sigma_x \sigma_y}$ where, σ_x and σ_y represents beam sizes at the viewers in x and y directions, respectively. The photogun bias voltage was 300 kV with laser settings adjusted to provide a low bunch charge beam that was not impacted by space charge forces: 1 fC bunch charge, 50 ps (FWHM) pulse width, and 0.3 mm rms laser spot size.

Fig. 9 shows the beam size measurements at each of the three YAG viewer screens over the entire range of the solenoid magnetic field with maximum field at the photocathode 0.15 T. GPT beam size predictions are also included for comparison. Overall, there is very good agreement between measured and predicted beam sizes at each viewer. Note, 3%, 5%, and 7% errors were assigned to beam size measurements for viewers 1, 2, and 3, respectively, to account for fluctuations in beam stability and possible beam loss. Instrumental errors, i.e. due to camera resolution are negligible when compared to beam jitter. For GPT simulations, systematic error analysis was conducted by identifying possible sources (e.g., laser instability, uncertainty in assigning photocathode mean-transverse energy (MTE), and imprecise knowledge of B_z along the beamline) and assigning reasonable error bars. Finally, it was important to consider the exact position of the photocathode surface relative to the back face of the photogun cathode electrode. After experiments described in this report, we found the photocathode recessed by ~1 mm from its ideal intended position [48], which resulted in additional Pierce-electrode focusing of the beam.

Notice in Fig. 9 how beam size at each of the viewers grows and shrinks with the magnetic field, a behavior known as mismatch oscillations [25]. The magnetic force from the cathode solenoid, with its non-uniform magnetic field near the photocathode, as shown in Fig. 10, does not match the initial emittance force, and these imbalanced forces result in repeated focusing of the beam within the solenoid [25,55]. The radial equation of motion provides added insight [25] (for simplicity, we assume here there is no axial electric field components, i.e., $\gamma' = \gamma'' = 0$, in other words, this equation is only valid outside the gun (z > 0.09 m));

$$r'' + \left(\frac{eB}{2mc\beta\gamma} \right)^2 r - \left(\frac{p_\phi}{mc\beta\gamma} \right)^2 \frac{1}{r^3} = 0, \qquad (5)$$
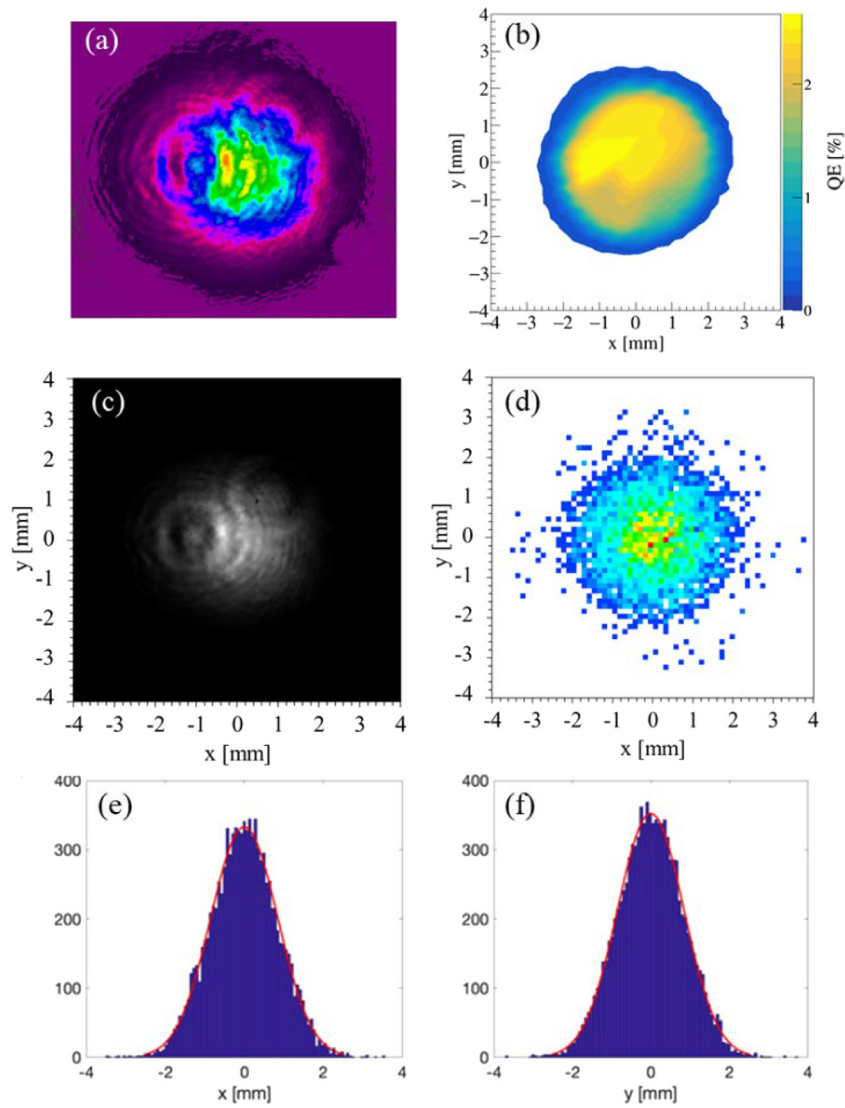
Fig. 7. (a) Laser profile. (b) QE profile. (c) GPT input gray scale image from the laser profile weighted by the QE profile. (d) Initial electron distribution from the laser profile weighted by the QE profile. (e) *x*-distribution at the photocathode with Gaussian fit. (f) *y*-distribution at the photocathode with Gaussian fit.
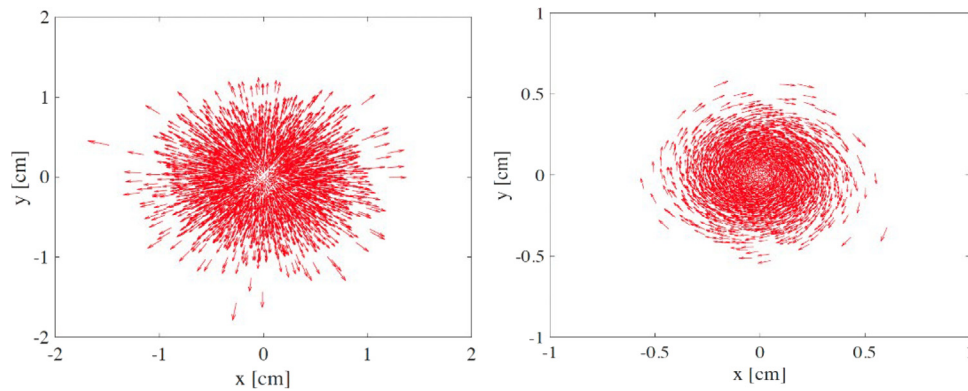

Fig. 8. Motion of the non-magnetized divergent beam (left) and magnetized beam (right). The random thermal motion of the individual electrons is relatively very small to display. Displayed beam sizes are typical for conditions described below.

where r'' represents the change of slope of the particle trajectory, c is the speed of light, and β is the Lorentz factor. The second term represents the transverse confining force from the magnetic field and the third term represents the centrifugal de-confining force due to the

canonical angular momentum p_ϕ;

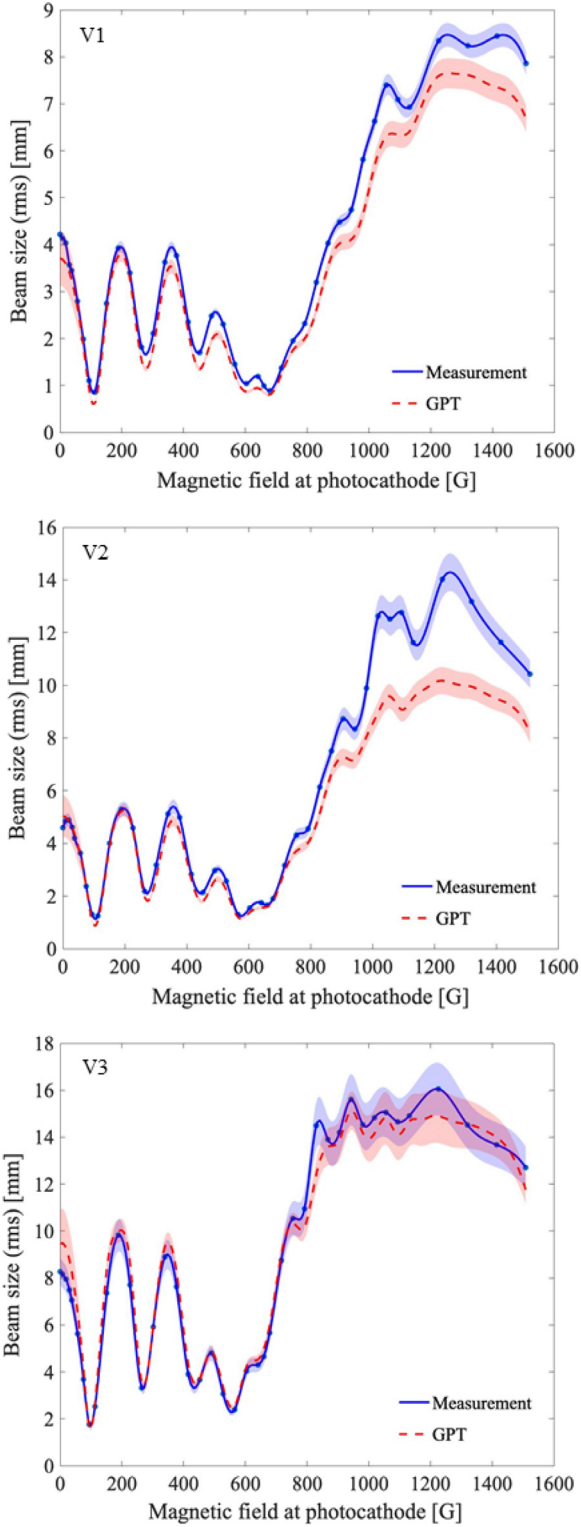$$p_\phi = \frac{eB_0 r^2}{2} = \omega_L (z = 0) \gamma m r^2.$$ (6)

Fig. 9. Beam size (rms) variation at each of the three viewers as a function of the magnetic field at the photocathode. For these measurements the beamline solenoids were not powered.

When $\omega'_L = 0$, corresponding to a longitudinally uniform magnetic field, $\omega_L(z) = \omega_L(0)$. Hence the confining and de-confining terms cancel, $r'' = 0$ and particles move along the field lines. However, when $\omega'_L \neq 0$, the confining and de-confining terms do not cancel ($\omega_L(z) \neq \omega_L(0)$) and

mismatch oscillations occur,

$$r'' + \left(\frac{\omega_L(z)}{\beta c}\right)^2 r - \left(\frac{\omega_L(z=0)}{\beta c}\right)^2 r = 0. \tag{7}$$

This same radial equation of motion, through an envelope-type analysis, gives the evolution of the rms beam size in simulations as illustrated in Fig. 10. The figure shows predicted electron beam size starting from the photocathode and along a section of the diagnostic beamline dominated by the cathode solenoid magnetic field, for a wide range of solenoid currents. In all instances, the electron beam size oscillates compared to the smooth beam size profile associated with no applied magnetic field (blue curve), showing only the focusing of the beam due to the Pierce electrode geometry.

4.2. Rotation angle variation with the magnetic field at the photocathode

The rotation angle (shearing angle) of the magnetized beam was measured as a function of applied magnetic field at the photocathode. The rotation angle was obtained by inserting a slit at the location of the first YAG viewer screen and measuring the corresponding beamlet angle at the second and third YAG viewer screens (referred to as "slit 1 to viewer 2", and "slit 1 to viewer 3", respectively), and by inserting a slit at the second YAG viewer screen location and measuring the rotation angle at the third YAG viewer screen ("slit 2 to viewer 3"). The rotation of the magnetized beam is not purely radial (angular momentum would then be zero), nor purely azimuthal (since there is only a small longitudinal magnetic field at the locations of viewers), but it is the result of both radial and azimuthal expansions.

The simulations were done using the GPT program employing the same parameters as before. A virtual slit was created at each slit location, and the electrons were numerically tracked to the downstream YAG viewer screens assuming the two momentum components p_x and p_y are constants for each electron after they exit electromagnetic fields since no additional forces are acting on them afterward. Linear fits were done for the slit image at the slit location and the viewer location. The rotation angle was calculated from the gradients of the two fits.

Fig. 11 shows the measured beamlet rotation angles and predictions from GPT simulations, versus magnetic field at the photocathode for the three possible measurement conditions: "slit 1 to viewer 2", "slit 1 to viewer 3", and "slit 2 to viewer 3" together with the beam size variations presented previously in Fig. 9, and presented again to highlight the important correspondence between rotation angle and beam size.

In all instances, beam size minima correspond to more beamlet rotation (correlation denoted by vertical dashed lines). This shows the conservation of angular momentum: as the beam expands, its angular velocity decreases resulting in smaller rotation angles. Though there is good overall agreement between measurement and simulation, measurements indicate more rotation than predicted by simulation for solenoid fields in the range of 566 and 660 G. This could be a result of the too small beam size and thus the small beamlet at each measurement location, making the measurements harder and less certain. The error analysis was done the same way as described previously.

Next, we compare and contrast the magnitude and sign (positive or negative) of the rotation angles shown in Fig. 11. In our setup, the direction of the longitudinal magnetic field at the photocathode is in the $+z$ direction, which when considered alone, should yield a clockwise rotation of the beamlet (i.e., negative angular velocity). As the beamlet propagates downstream of the slit, because the vertical velocity is linearly correlated with the horizontal position, the beamlet will rotate into the 4th quadrant of the Cartesian plane, ultimately to $-90°$, as the propagation distance gets larger and larger. This is illustrated in Fig. 12 which shows beamlet rotation into the 4th quadrant for all three slit-viewer combinations. There was however one condition when the beamlet was observed to rotate past $-90°$ (i.e., into the 3rd quadrant) and a range of conditions that provide positive rotation angles (i.e., in
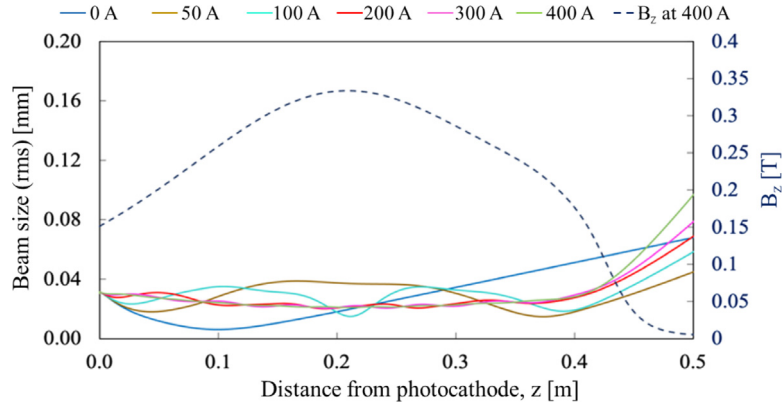
Fig. 10. Predicted electron beam size (rms) from GPT simulation showing mismatch oscillations inside the cathode solenoid (first 0.5 m of the beam path).
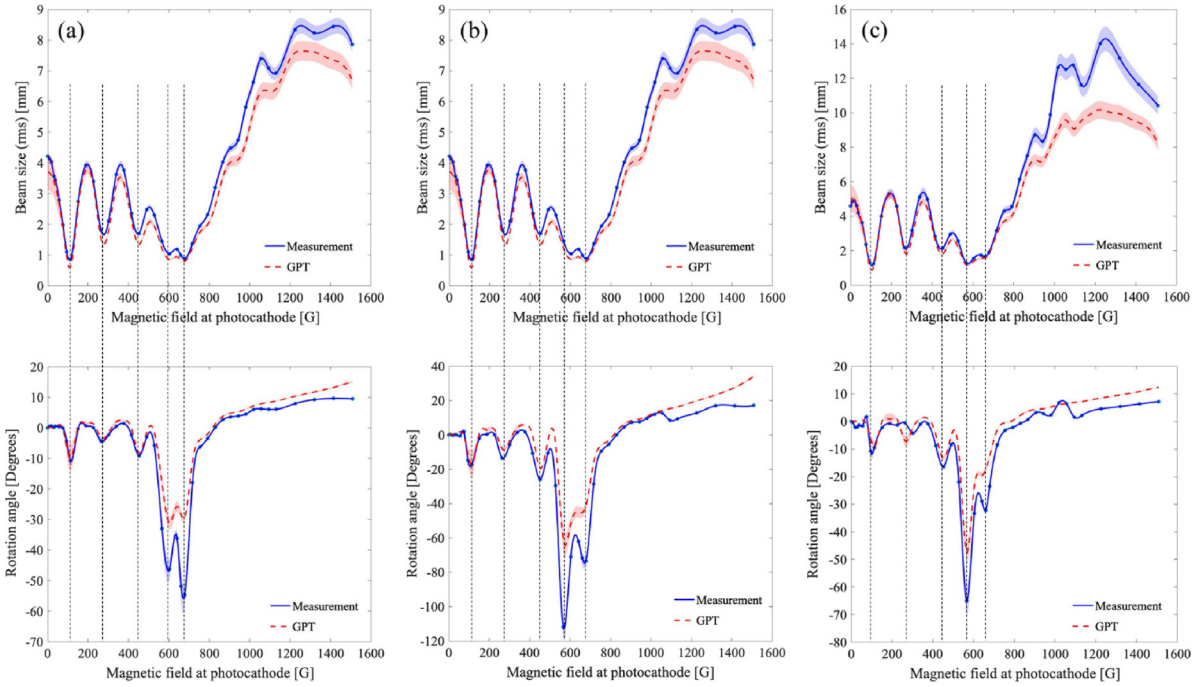

Fig. 11. Beam size (rms) variation and beamlet rotation angle versus magnetic field at the photocathode: (a) beam passing through slit 1 and evaluated at viewer 2, (b) beam passing through slit 1 and evaluated at viewer 3, (c) beam passing through slit 2 and evaluated at viewer 3.

1st quadrant), as shown in Fig. 13. Explanations for these behaviors follow.

Note that as shown in Fig. 4, a mirror behind the viewer screen at 45° reflected the beam image outside the beamline. Then a second mirror on the side of the beamline reflected the image down to a camera mounted on the floor. The second mirror caused right–left image reversal. GPT uses right-handed coordinate system (beam propagates along $+z$, $+y$ is up, and $+x$ is beam left). For measurements and GPT, $+x$ is beam left as indicated in Figs. 12 and 13. Both figures are presented as if we look at the beam head.

The large variation in rotation angles, covering multiple quadrants, can be explained by examining Eq. (8) as derived in Ref. [56], which predicts the rotation angle, ϕ_{rot}, as a function of distance z between the slit and viewer, and the beam parameters at each slit,

$$\phi_{rot} = atan2\left(\frac{\dot{\phi}z/v_z}{1 - z/f}\right), \tag{8}$$

where $\dot{\phi}$ is the angular velocity at the slit, v_z is the velocity in z direction, f is the focal length of the beam envelope, and the inverse trigonometric function $atan2\,(y/x)$ returns the four-quadrant inverse

tangent of its variables y and x. With $x' = -\frac{x_{0,rms}}{f}$ and $\alpha\epsilon = -\langle xx'\rangle$, $\frac{1}{f} = \frac{\alpha\epsilon}{x_{0,rms}^2}$ where $x_{0,rms}$ is the beam size at the slit, α is the Twiss parameter that describes the beam convergence/divergence, and ϵ is the transverse rms emittance [57]. Then Eq. (8) becomes

$$\phi_{rot} = atan2\left(\frac{\dot{\phi}z/v_z}{1 - \frac{z\alpha\epsilon}{x_{0,rms}^2}}\right). \tag{9}$$

Fig. 14 shows GPT predictions of Twiss parameter α as a function of the solenoid magnetic field at slits 1 and 2. At slit 1, α is always negative, which describes a diverging beam. At slit 2, α is negative except for a narrow range of photocathode magnetic fields between 547 and 588 G.

The GPT predictions of Twiss parameter α at slits 1 and 2, together with Eq. (9), were then used to calculate the beamlet angular velocity, $\dot{\phi}$. The change in rotation direction seen in Fig. 15 when the beam size becomes very large, can be explained by noting that the magnetic field of the cathode solenoid extends along the entire beamline, and by examining the conservation of canonical angular momentum in Eq. (1). Consider a beam inside the cathode solenoid where $B_z = B_0$, $\dot{\phi}_1 = 0$
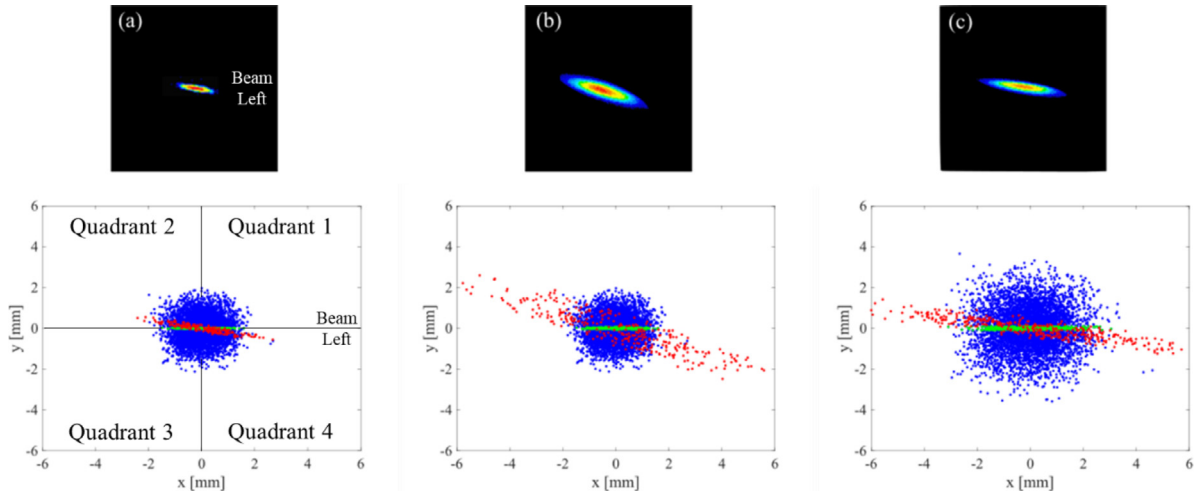
Fig. 12. The beamlet is observed to rotate clockwise for low current applied to the solenoid: (a): slit 1 - viewer 2, (b): slit 1 - viewer 3, (c): slit 2 - viewer 3 for photocathode magnetic field 113 G. Top images show the measured beamlet created by passing beam through a slit, and viewed on downstream YAG viewer screen. Bottom images are the corresponding simulation results. Blue dots represent beam profile at the slit location, the green dots represent the beamlet produced by the slits, and the red dots represent the predicted beamlet at the location of the referenced viewer.
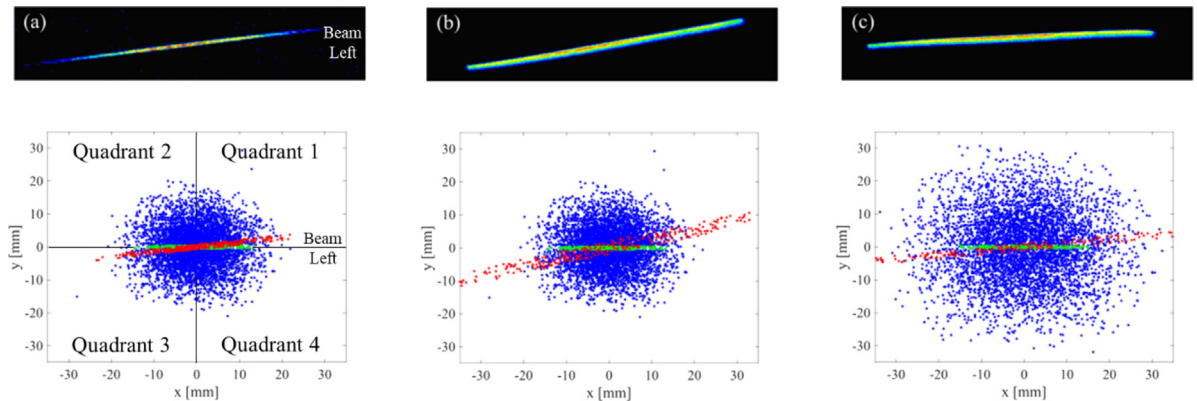
Fig. 13. The beamlet is observed to rotate counterclockwise for high current applied to the solenoid: (a): slit 1 - viewer 2, (b): slit 1 - viewer 3, (c): slit 2 - viewer 3 for photocathode magnetic field 1132 G. Top images show the measured beamlet created by passing beam through a slit and viewed on downstream YAG viewer screen. Bottom images are the corresponding simulation results. Blue dots represent beam profile at the slit location, the green dots represent the beamlet produced by the slits, and the red dots represent the predicted beamlet at the location of the referenced viewer.
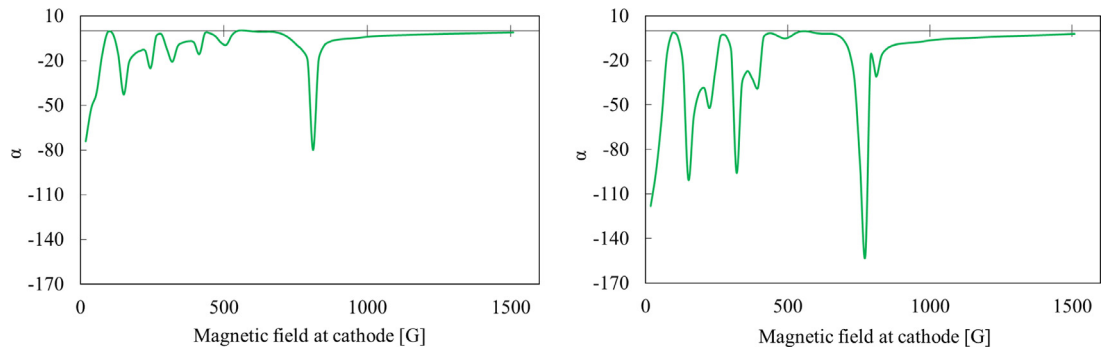

Fig. 14. Twiss parameter α variation at slit 1 (left) and at slit 2 (right) from GPT simulation. For slit 1, α is negative for all photocathode magnetic fields except 547–588 G and for slit 2, α is always negative.
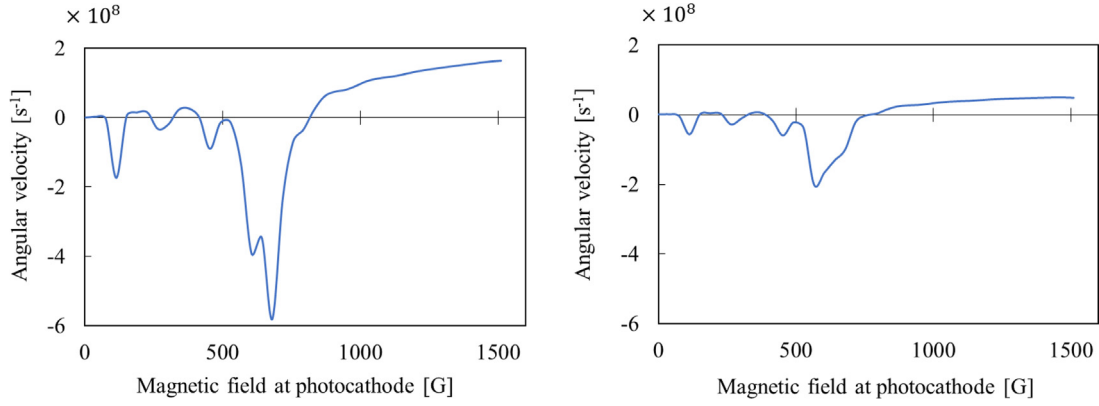
Fig. 15. The angular velocity variation as a function of the photocathode magnetic field at slit 1 (left) and at slit 2 (right) from GPT simulation showing negative (clockwise, CW) and positive (counterclockwise, CCW) velocities.

Table 2
Explanation of the magnitude and the sign (positive or negative) of the rotation angles shown in Fig. 11 and their quadrants.

Slit #	Magnetic field at photocathode [G]	α	Angular velocity, $\dot{\phi}$ [s^{-1}]	Rotation angle quadrant
1	0–547, 588–1509	Negative (diverging)	Negative (CW) Positive (CCW)	4th 1st
	547–588	Positive (converging)	Negative (CW)	4th for viewer 2 3rd for viewer 3 (determined by z, α, ϵ, and $x_{0,rms}$)
2	0–1509	Negative (diverging)	Negative (CW) Positive (CCW)	4th 1st

and outside the solenoid where $B_z = B_1$, $\dot{\phi}_1 \neq 0$, $B_1 << B_0$. Beam size inside the solenoid is r_0 and outside the solenoid is r_1. From Eq. (1), the angular velocity can be re-written as [25],

$$\dot{\phi}_1 = \frac{e}{2\gamma m} \left[B_1 - B_0 \left(\frac{r_0}{r_1} \right)^2 \right]. \tag{10}$$

According to the above equation, $\dot{\phi}_1$ is negative except when the beam size outside the solenoid becomes very large ($r_1 >> r_0$).

The observations of beamlet rotation, together with information gleaned from Figs. 14 and 15, are summarized in Table 2.

4.3. Conservation of canonical angular momentum

The canonical angular momentum of the electron beam moving in longitudinal magnetic field can be obtained by averaging Eq. (1) over the beam distribution,

$$\langle \mathcal{L} \rangle = \gamma m \langle r^2 \dot{\phi} \rangle + \frac{1}{2} e B_z \langle r^2 \rangle, \tag{11}$$

and using $\langle r^2 \dot{\phi} \rangle = \langle x v_y - y v_x \rangle$. To verify conservation of canonical angular momentum, GPT simulations were conducted with similar beam parameters used in beam size and rotation angle simulations described above, and using weighted laser spatial and QE profiles.

According to GPT simulations, there is conservation of canonical angular momentum provided there is no beam loss along the beamline. This is illustrated in Fig. 16: canonical angular momentum of the beam at viewer 2 is equal to the canonical angular momentum of the beam at the photocathode as long as electrons remain inside the magnetic field map of the region and contained by the beam pipe radius. For solenoid magnetic fields between 754 and 1509 G, corresponding to angular momentum in the range ~9 to 14 neV s, beam size exceeds the diameter of the beampipe at viewer 2 and as such, canonical angular momentum is not conserved.

Experimentally, we were unable to demonstrate the conservation of the canonical angular momentum from measurements of beam sizes
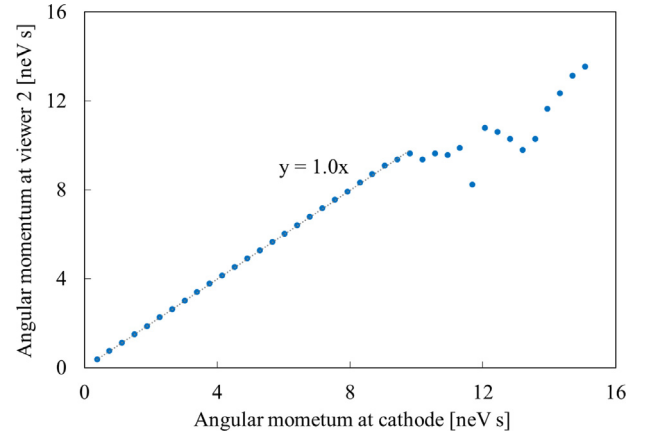

Fig. 16. Canonical angular momentum at viewer 2 vs. canonical angular momentum at the photocathode inferred from the magnetic field, as predicted from GPT simulation.

and rotation angles not only because of beam loss but also because we only measured the rotation of the beamlet and not the whole beam. The beamlet was not representative of the whole beam because the whole beam was not a perfect Gaussian but rather a non-uniform distribution resulting from the complicated laser and QE profiles. Furthermore, we only measured the average beam size instead of $\langle r^2 \dot{\phi} \rangle$. However, measurements of the correlated emittance were possible and indicate the conservation of the canonical angular momentum, as described in the next sub-section.

4.4. Correlated emittance variation with the magnetic field at the photocathode

According to Busch's theorem, electrons born inside a magnetic field will acquire mechanical angular momentum in the field free
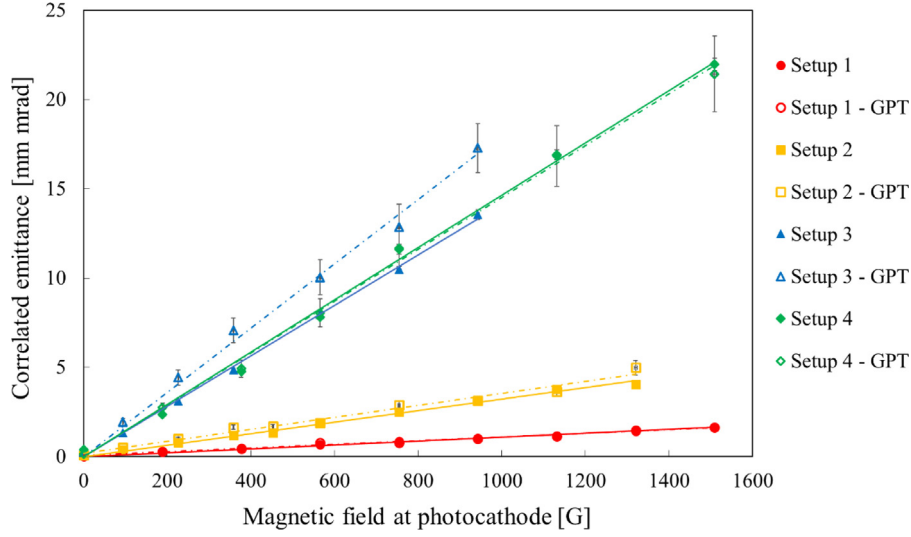
Fig. 17. Correlated emittance measurements and corresponding GPT simulations as a function of magnetic field at the photocathode. For setup 1, the measurements and simulations lie on top of each other. The slopes of linear fits are summarized in Table 3.

region which increases the emittance of the electron beam. This new emittance is referred to as the drift or correlated emittance, $\epsilon_{correlated}$. The total normalized transverse emittance associated with the angular momentum dominated beam is then given by [58];

$$\epsilon_{n,rms} = \sqrt{\epsilon_{correlated}^2 + \epsilon_{uncorrelated}^2},\tag{12}$$

where the uncorrelated emittance $\epsilon_{uncorrelated}$ combines the effect of thermal and non-linear space charge components and the correlated emittance $\epsilon_{correlated}$ represents the magnetization which is given by [25];

$$\epsilon_{correlated} = \frac{\langle L \rangle}{2mc} = \frac{eB_0\langle r^2 \rangle}{4mc}.\tag{13}$$

The photocathode thermal emittance per rms laser spot size was measured to be ∼0.4 mm mrad/mm [43]. Thus, knowing the uncorrelated emittance, and measuring the normalized emittance, allows the determination of the correlated emittance.

The normalized emittance was measured using the solenoid scan technique [59]. Before the measurements, beam was centered throughout the beamline and delivered to the dump. The first two focusing solenoids were used to make a small beam to eliminate beam loss. The third focusing solenoid was used as the scanning solenoid with the beam size measured at the third viewer. At the location of the third focusing solenoid, the magnetic field from the cathode solenoid becomes very small. So, by making the beam size small, the beam has only mechanical angular momentum and the conservation of the canonical angular momentum relates the measured correlated emittance to the magnetic field and beam size at the photocathode [Eq. (13)]. Four different laser sizes were used and the emittance measurements were taken for different magnetic fields at the photocathode from 0–1509 G. For these measurements, we extracted beam with 1 fC bunch charge to eliminate space charge effects.

GPT was used to simulate the results. The 3D electric field map of the photogun and the 2D magnetic field map of the gun solenoid were used in the simulations. Similarly, the GPT "GDFMGO" program optimized the steering magnets to keep the beam on-axis throughout the beamline [42]. Also, as before, the weighted laser profiles were generated for each laser and QE combination and used as the initial electron distribution. Table 3 shows the different setups and the initial electron beam size rms values obtained from each Gaussian fit.

GPT rms emittance routines, "nemixrms" and "nemiyrms", were used to obtain the total emittances along the beamline. Further, "nemirrms" routine was used to obtain the uncorrelated emittance. The

uncorrelated emittance was calculated by removing the $r - p_\phi$ coupling due to the solenoid field from the normalized emittance [60] (see Appendix).

Fig. 17 shows the correlated emittance measurements (after subtracting the thermal emittance from the measured normalized emittance) and corresponding GPT simulations. There is a clear linear dependence of the correlated emittance on the applied magnetic field at the photocathode, consistent with Eq. (13). Table 3 shows that measurement and simulation exhibit better agreement at 300 kV. At the lower gun HV, beam transport is more challenging and beam loss removes electrons from the peripheral extent of the beam. These electrons have larger mechanical angular momentum and thus have the most contribution to the correlated emittance. It was difficult to measure large beam sizes at the higher magnetic field strengths, and larger error bars were assigned to these measurements. For GPT simulations, as before, systematic error analysis was conducted by identifying possible sources (e.g., laser instability, uncertainty in assigning photocathode mean-transverse energy (MTE), and imprecise knowledge of B_z along the beamline) and assigning reasonable error bars.

4.5. High current runs

Photocathode lifetime was studied by delivering high current magnetized beams to the dump. Magnetized beams pose additional challenges when compared to non-magnetized beams due to a significant increase in beam size due to the additional correlated emittance when exiting the cathode solenoid, which can cause beam loss and degraded vacuum levels. Although multi-alkali cathodes are very robust, degraded vacuum can still cause degradation of the QE [43,61].

The photocathode QE charge lifetime is defined as the amount of charge extracted before the QE falls to $1/e$ of its initial value;

$$QE = QE_0 e^{-C/\tau},\tag{14}$$

where C is the charge extracted and τ is the charge lifetime in Coulomb. Table 4 lists the beam parameters and the measured lifetimes of various conditions explored. The first run in the table was delivered from a photocathode grown on GaAs substrate with 10 min Sb deposition while all the other runs were delivered from a photocathode grown on Mo substrate with 10 min Sb deposition.

The highest magnetized beam current produced was 28 mA with a cumulative extracted charge of 5200 C and an estimated $1/e$ charge lifetime of 9400 C. For this run, the diode-based laser and fiber amplifier

Table 3
Gun HV and initial beam size at the photocathode for each setup. The results of linear fits to both the measurements and GPT simulations are also summarized.

Setup	Beam size (rms) at photocathode [mm]	Gun HV [kV]	Measurement $\frac{\epsilon_{correlated}}{B_0}$ [mm mrad/G]	GPT $\frac{\epsilon_{correlated}}{B_0}$ [mm mrad/G]
1	0.22	300	0.00109 ± 0.00002	0.00109 ± 0.00003
2	0.43	200	0.00322 ± 0.00005	0.00356 ± 0.00011
3	0.84	200	0.0141 ± 0.0001	0.0180 ± 0.0003
4	0.76	300	0.0146 ± 0.0002	0.0145 ± 0.0002

Table 4
Beam parameters for high current runs and measured charge lifetimes. Photocathodes grown on Mo substrate were used for all the runs except the first run when the photocathode was grown on GaAs substrate.

| Electron beam current [mA]	Gun HV [kV]	Magnetic field at photocathode [G]	Laser spot size, rms [mm]	Laser repetition rate [MHz]	Laser pulse width, FWHM [ps]	Bunch charge [pC]	Run time [hour]	Charge extracted [C]	Charge lifetime [C]
4.5	300	1514	0.4	DC	–	–	6	100	164
4.5	200	757	0.9	374.25	50	12	38	620	No QE decay
14	200	0	0.9	303.30	60	46	16	880	No QE decay
14	200	757	0.9	303.30	60	66	92	4500	No QE decay
20	100	568	0.9	303.30	60	66	22	1440	No QE decay
28	100	568	1.4	374.25	50	75	57	5200	9400
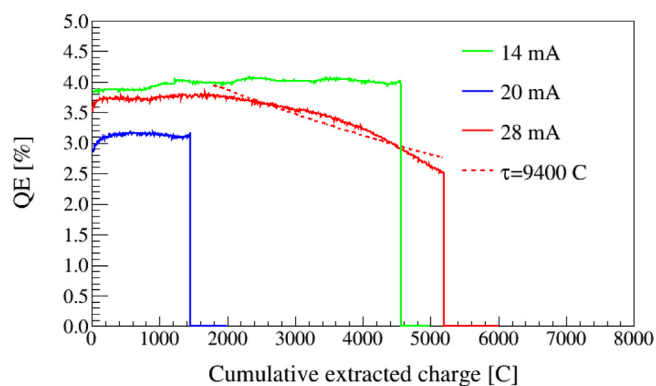
Fig. 18. QE vs. cumulative extracted charge for magnetized beam delivery at three different average currents. The dashed line shows a fit to the 28 mA run according to Eq. (14) with a charge lifetime of 9400 C.

Fig. 19. Beam current variation with the time for magnetized beam delivery at three different average currents.

system was used with a 1.4 mm (rms) laser spot size, 50 ps (FWHM) pulse width and 374.25 MHz repetition rate. The photocathode magnetic field was set to 568 G. The bunch charge of the beam was 75 pC. Note, the photogun high voltage power supply used for the high current runs was limited to 3 kW power. As such, to deliver 28 mA, the photogun bias voltage was reduced to 100 kV.

The first run listed in Table 4 was taken with a photocathode grown on GaAs substrate with 10 min Sb deposition: it provided the smallest charge lifetime. All the other runs employed a photocathode grown on a Mo substrate with 10 min Sb deposition. For these runs, QE decay was observed only for the highest current at 28 mA (Fig. 18). Runs at lower current showed no measurable QE decay.

According to previous work [43], ionized residual gas striking the photocathode (ion back bombardment), and chemical desorption due to heating caused by the high laser power needed to deliver high beam currents, are the dominant mechanisms for photocathode QE decay. The superior charge lifetime achieved from the sample prepared on the Mo substrate, which has high thermal conductivity, supports the theory that minimizing heating is essential for continuous delivery of high current beams from an alkali-antimonide photocathode [44]. For the 28 mA run (which initially started as 26 mA run), the downward trend in beam current seen in Fig. 19 after 24 h is likely due to photocathode heating and associated bandgap shift [62], or chemical changes (due to preferential evaporation of Cs), both of which indicate the need for photocathode cooling for high average current delivery. Another possibility is enhanced ion bombardment due to worsening vacuum due to beam halo at this very high beam current. Although not studied
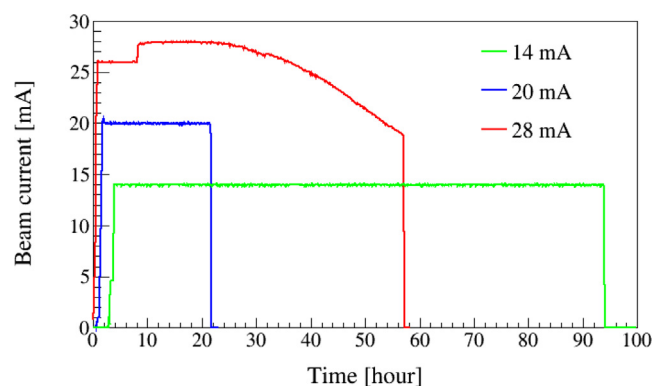
as thoroughly as in ref [61], there was indication that the cathode solenoid magnetic field and the biased anode (+1000 VDC) helped prevent beamline ions from entering the gun, and possibly helping to prevent high voltage arcing inside the gun that sometimes resulted in stepwise decrease in QE.

5. Characterization of the space charge dominated magnetized electron beam

Next, we attempted to extract high bunch charge from the magnetized photogun, to explore the interplay between space charge effects and magnetization. We note that *space charge effects* represent a complicated set of processes including the Coulomb repulsive forces that change the electron bunch dimensions and impact beam transport, Child's Law [63–68] also known as the space charge limit, and the possibility of photocathode phenomena, such as surface charge limit [69–72]. However, as described below, we were handicapped by beam loss – related to large magnetized beam sizes, made even larger by the space charge forces – and exacerbated by the fact that we had to run at lower gun high-voltage due to problematic field emission.

Magnetized beam at high bunch charge was produced using a pulsed commercial laser. The laser pulse repetition rate was $f = 50$ kHz and the optical pulse width was set to 75 ps (FWHM). Laser power was increased in small steps from 0 to a maximum of 30 mW while monitoring the beam current delivered to the dump. Laser pulse energy was calculated by dividing the measured laser power at the entrance of the gun by f. The bunch charge, Q, was calculated using the measured average beam current at the dump and knowing the laser pulse
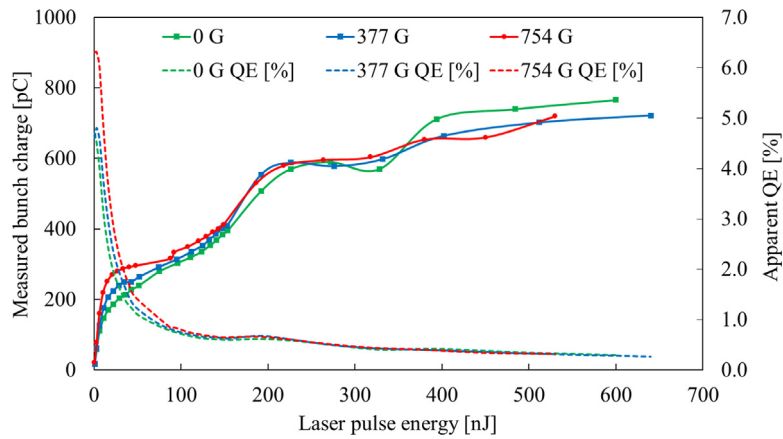
Fig. 20. Bunch charge (calculated using the average beam current measured at the dump) vs. laser pulse energy and the corresponding apparent QE for cathode solenoid magnetic fields 0, 377, and 754 G. Photogun bias voltage was 225 kV.

repetition rate ($Q_= I_{avg}/f$). The apparent QE was calculated using the average beam current at the dump and the incident laser power. The gun operated at high voltages up to 225 kV, lower than typical because field emitters appeared after operating for a while at very high voltage. The anode was biased at +1000 VDC.

In this section the "measured bunch charge" is what we measured at the dump. The "initial bunch charge" is the bunch charge used in GPT simulations and calculated using the measured initial QE at low electron beam current and laser pulse energy. The "expected bunch charge" is the result from GPT simulations at different locations along the beamline.

5.1. As a function of magnetic field at the photocathode

At low bunch charge and average current, the focusing solenoids and steering magnets were adjusted to optimize beam transport to the dump, to maximize the measured dump average beam current (I_{avg}). Fig. 20 shows the measured bunch charge and the apparent photocathode QE calculated using the average beam current measured at the dump, as a function of laser pulse energy, for cathode solenoid magnetic fields 0, 377, and 754 G. The photogun bias voltage was 225 kV.

For each cathode solenoid magnetic field, the apparent QE falls rapidly with increasing laser power. For laser pulse energy ~10 nJ, there is the hint of a plateau in delivered bunch charge, especially for the 754 G cathode solenoid condition, suggesting the Child's law space charge limit was reached at ~300 pC. Higher bunch charge could still be extracted, but the charge exceeding ~300 pC likely originates from the edge of the laser profile. The oscillatory behavior seen at higher pulse energies likely stems from mismatch oscillations and related beam loss. The limited beamline aperture and insufficient strength of the focusing solenoids prevented clean transport of the beam to the dump.

During tests at high bunch charge, beam loss was frequently very significant as indicated by the beamline ion pumps which registered higher operating current. The real QE dropped from 6.3% to 4.7% following measurements with the gun solenoid set to provide 754 G at the photocathode. Since the anode was biased during these measurements – repelling ions produced downstream of the anode – the QE reduction likely stems from beam loss within the gun, on the anode electrode. Unmistakable evidence of beam loss, both at the anode and along the beamline, highlights the problem of the present setup in terms of measuring the extracted bunch charge and real photocathode QE. Calculating the bunch charge and QE using measured average dump current values was not reliable when the electron beam size became so large that significant beam loss occurred, but the present test conditions provide no alternative.
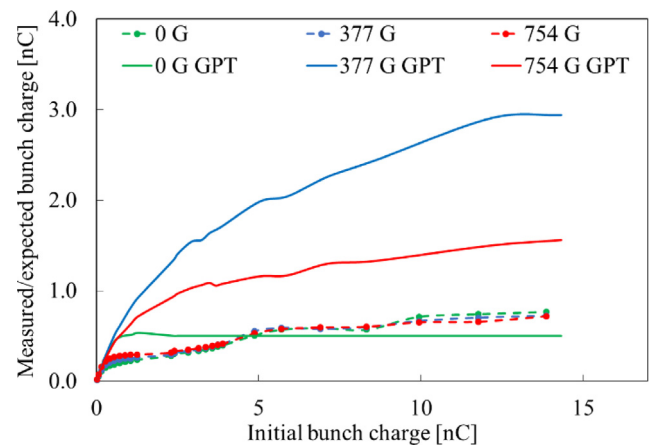

Fig. 21. Measured bunch charge at the dump vs. expected bunch charge from GPT for 0, 377 and 754 G cathode solenoid magnetic fields under these conditions: 225 kV, 50 kHz, 75 ps (FWHM), 1.2 mm rms laser spot size.

Simulations of high bunch charge magnetized beam were performed using GPT. The "GDFMGO" solver program was used for steering magnet optimization to maximize charge extraction and to center the beam throughout the beamline [42]. The simulation parameters mimicked the test conditions including the fields of the beamline solenoids and the beam pipe radii. As before, a grayscale bitmap image of the laser profile weighted by the real QE profile was implemented as the initial electron distribution since all the laser spots were not proper Gaussian.

Fig. 21 presents delivered charge measured at the dump – the same data as shown in Fig. 20 – but plotted as a function of the initial bunch charge, together with the corresponding GPT simulation results for different magnetic fields at the photocathode. For the non-magnetized beam condition (0 G) there is modest agreement between simulation and measurement but very poor agreement for magnetized beam (377 and 754 G). The GPT simulation predicts much higher charge extraction when the cathode solenoid is energized, a prediction not observed by measurements. Both of these observations will be discussed next.

Particle tracking results shown in Fig. 22 illustrate the simulated particle trajectories (left) and the beam loss along the beamline for 0, 377, and 754 G cathode solenoid magnetic fields (right). The cathode solenoid serves to quickly capture and focus the beam, improving transmission to the dump, but because of mismatch oscillation described above in Section 3, much higher beam extraction was estimated for cathode solenoid magnetic field at 377 G than 754 G.

Fig. 23 shows GPT predictions of delivered charge for different cathode solenoid magnetic fields at three beamline locations: 1 cm from the
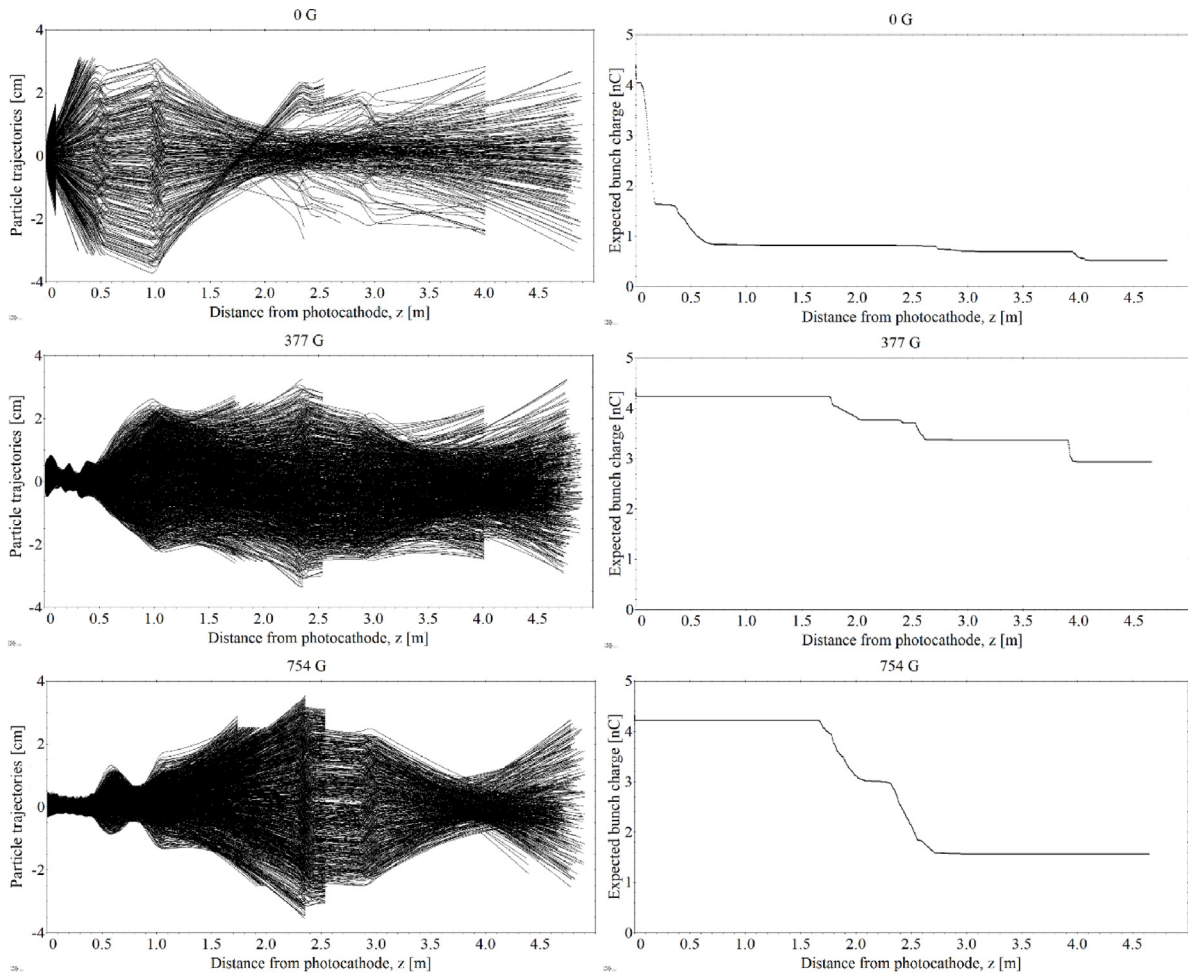
Fig. 22. Particle trajectories (left) and beam loss (right) along the beamline for cathode solenoid magnetic fields 0, 377, and 754 G. The anode aperture diameter is 2 cm (at z = 0.09 cm) and beamline diameter varied between 5 and 7 cm. (225 kV, 50 kHz, 75 ps (FWHM), 14 nC, 1.2 mm rms laser spot size).

photocathode, after the anode, and at the dump, with gun bias voltage 225 kV, 75 ps (FWHM) laser pulse width, 1.2 mm (rms) laser beam size, 6 nC initial bunch charge, and with focusing solenoids optimized for maximum charge delivery. At 1 cm from the photocathode, charge extracted is the same for all solenoid magnetic fields, implying the charge extracted does not depend on the magnetization strength, at least as indicated by GPT simulations. The GPT simulations predict significant beam loss at the anode electrode for cathode solenoid magnetic fields less than 200 G. At the dump, GPT predicts significant variation in measured charge due to mismatch oscillations, with the highest transmission obtained for cathode solenoid magnetic fields between 300 and 500 G. Importantly, GPT predicts there are no magnetized beam conditions at the GTS that provide 100% transmission to the dump, at least with the photogun biased at only 225 kV. Finally, it must be said these simulations do not explain the near identical results shown in Fig. 21, with maximum delivered charge of 0.7 nC for each magnetized beam condition tested. In general, whereas measurements and GPT simulations showed excellent agreement at low bunch charge, this agreement disappeared during the high bunch charge tests and this was likely a result of excessive beam loss along the entire beamline and even near the photocathode itself.

5.2. As a function of gun voltage and bunch dimensions

According to Child's law [63–68], the charge extracted from the photocathode is limited by the gun high voltage, and the spatial and temporal dimensions of the electron beam (which are related to laser
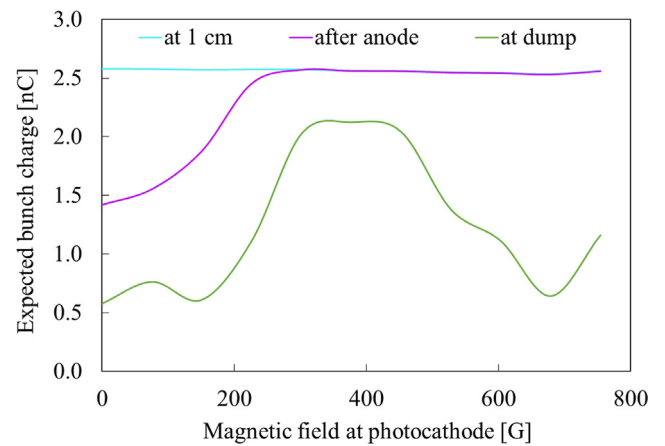

Fig. 23. GPT simulations of expected bunch charge delivered to three different beamline locations as a function of magnetic field at the photocathode; 1 cm from the photocathode, downstream of the anode, and at the beam dump. These simulations were done under these conditions: 225 kV, 75 ps laser pulse width (FWHM), 1.2 mm rms laser spot size, and 6 nC initial bunch charge.

beam size and pulse width). Hence, the above experimental procedure was repeated using various gun high voltages, laser spot sizes at the photocathode, and laser pulse widths, for non-magnetized and magnetized beams. As mentioned previously, the photogun developed field
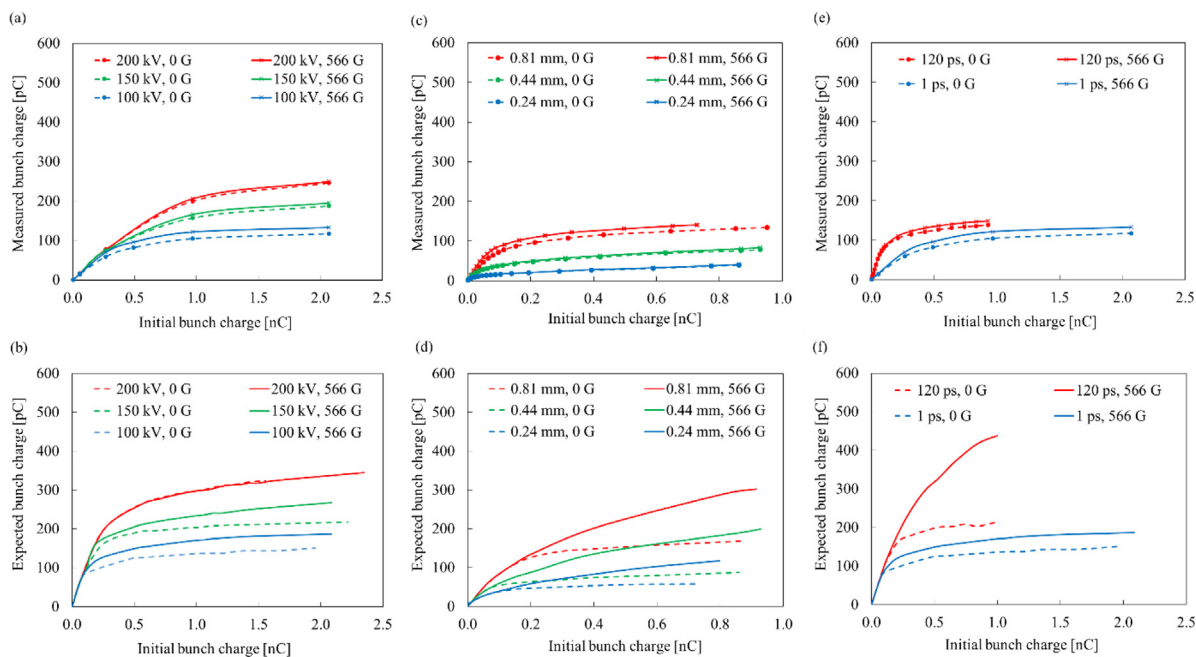
Fig. 24. (a) Measured bunch charge vs. expected bunch charge and (b) corresponding GPT simulations for different gun high voltages for magnetized and non-magnetized beam (1 ps (FWHM), 1.54 mm (rms)). (c) Measured bunch charge vs. expected bunch charge and (d) corresponding GPT simulations for different laser spot sizes for magnetized and non-magnetized beam (100 kV, 70 ps (FWHM)). (e) Measured bunch charge vs. expected bunch charge and (f) corresponding GPT simulations for different laser pulse widths (FWHM) for magnetized and non-magnetized beam (100 kV, 1.54 mm (rms)).

emission which limited the gun bias voltage to 200 kV for this study. Simulations were performed using GPT software with the same beam parameters and initial electron beam distributions at the photocathode.

Fig. 24(a) illustrates the measured bunch charge vs. expected bunch charge and (b) corresponding GPT simulations for different gun high voltages for non-magnetized and magnetized beam (0 and 566 G, corresponding to 0 and 150 A solenoid currents). Both non-magnetized and magnetized beams show the expected results, namely, higher gun voltage permits the delivery of a higher bunch charge beam.

Coulomb repulsive forces inside a bunch are inversely proportional to its dimensions, *i.e.*, the transverse and longitudinal bunch sizes. Hence, the above experimental procedure was repeated using a variety of laser spot sizes (0.81, 0.44, and 0.24 mm), and laser pulse widths (1 and 120 ps (FWHM)) for non-magnetized and magnetized beam and corresponding simulations were performed using GPT software. Fig. 24(c) illustrates the measured bunch charge vs. expected bunch charge and (d) corresponding GPT simulations for different laser spot sizes for non-magnetized and magnetized beams (0 and 566 G). Fig. 24(e) illustrates the measured bunch charge vs. expected bunch charge and (f) corresponding GPT simulations for different laser pulse widths for non-magnetized and magnetized beams (0 and 566 G). Results are consistent with expectation for both beams, namely, by increasing the bunch dimensions, the space charge force can be suppressed to increase the extracted charge. As discussed before, GPT simulation predicts higher charge extraction when the cathode solenoid is energized (as the cathode solenoid quickly captures and focuses the beam, improving transmission to the dump and due to mismatch oscillations where for 566 G magnetic field at the cathode the beam is small throughout the transportation), a prediction not observed by measurements due to significant beam loss along the beamline which is very hard to simulate accurately.

6. Summary

A high current, high bunch charge magnetized electron source was successfully developed and commissioned at Thomas Jefferson National Accelerator Facility's Gun Test Stand. The magnetized beam source consists of a compact 300 kV DC high voltage photogun with an inverted insulator geometry and alkali-antimonide photocathode immersed in a magnetic field. Beam size variations showed an oscillatory behavior known as the "mismatch oscillations", due to the non-uniform magnetic field that extends over a substantial portion of the beamline, with some field regions serving to focus the beam, and other field regions defocusing the beam. This in turn affected the rotation angle, with large rotation angles observed for some cathode solenoid fields. The emittance associated with the magnetized electron beam (drift or correlated emittance) was studied and measured as a function of the magnetic field at the photocathode, laser spot size, and gun high voltage. Although loss at the higher magnetic field strengths prevented us from reaching the desired emittance values, the trend agreed with theoretical prediction. Beam size outside the cathode solenoid is related to the correlated emittance and thus, larger correlated emittance helps to reduce collective effects such as space charge blowup. A sustained high average current magnetized beam at average current up to 28 mA was demonstrated for a cathode solenoid magnetic field of 568 G with a cumulative extracted charge of 5 kC and an estimated $1/e$ charge lifetime of 9.4 kC. The superior thermal conductivity of the Mo substrate improved charge lifetime over the same photocathode grown on a GaAs wafer substrate. Further, this study showed that the applied magnetic field prevents arcing and stops beamline ions from entering the gun and contributing to the decay of the photocathode. High bunch charge magnetized beams up to 0.7 nC at 50 kHz repetition rate were also successfully generated, with clear indications of space charge limitations and significant beam loss. Table 5 summarizes the initial goals and what was achieved through this research.

The beamline was successfully modeled using GPT software by employing the electric field map of the photogun generated using CST Studio Suite's electromagnetic field solver and magnetic field map of the cathode solenoid generated using Opera software. MATLAB software was used as the post-processing tool. For beams at low bunch charge, simulations showed good agreement with measured values of the beam size, rotation angle, and correlated emittance. Simulations also verified the conservation of canonical angular momentum and provided explanations for observed mismatch oscillations, large rotation angles, and the direction of rotation (CW or CCW).

Table 5
Magnetized electron beam requirements and demonstrated results.

Parameter	JLEIC requirement	Demonstrated
Magnetic field at photocathode [T]	0.1	0.15
Bunch length [ps]	60 (Flat top)	1–120 (FWHM)
Repetition rate [MHz]	43.3	0.05, 303.30, 374.25
Laser spot radius [mm]	2.2 (Flat top)	1.4 mm (rms)
Normalized correlated emittance [mm mrad]	36	22
Average current [mA]	140 (at > 400 kV)	28 (50 ps (FWHM), 74.8 pC, 374.25 MHz, 100 kV, 570 G)
Bunch charge [nC]	3.2	0.7 (75 ps (FWHM), 50 kHz, 225 kV, 760 G)

To characterize space-charge dominated magnetized electron beam with nC bunch charge, measurements were made by varying the laser power and tracking the average current at the dump for different cathode solenoid magnetic fields. Space charge forces caused significant beam blowup, and the finite beamline aperture and insufficient strength of the focusing solenoids caused significant beam loss. Nearly identical results were obtained for three conditions (non-magnetized and two magnetized beam conditions): slightly improved transmission to the dump was obtained for bunch charge < ∼0.1 nC by increasing the magnetic field at the photocathode, but in all cases the maximum bunch charge delivered to the dump was ∼0.7 nC. In marked contrast, GPT simulations indicated that significantly more charge could be extracted with magnetized beam because of the added focusing provided by the gun solenoid. Simulations showed that the beam loss also depends on the cathode solenoid magnetic field due to the mismatch oscillations. But in terms of space charge forces, both measurements and simulations indicate that a magnetized beam behaves the same way as a non-magnetized beam: higher bunch charge can be extracted with higher gun voltage, larger laser beam spot size at the cathode, and long laser pulse width. Overall, this project provided insight but it also elucidates the challenges of magnetized beam production at high bunch charge. High bunch charge operation using a DC high voltage photogun represents the most significant challenge for a cooler design.

Future work will focus on the delivery of high bunch charge (a few nC) at higher gun voltages using a modified photogun with cathode/anode electrodes designed specifically for high bunch charge operation [48]. In addition, the beamline will be modified by removing and replacing some of the components with small apertures that cause beam loss. An insertable Faraday cup will be installed near the gun exit to more accurately determine the extracted current from the photocathode, to more accurately assess extracted bunch charge and photocathode QE. Another choice is to measure the current from the gun HV power supply, though this is a challenging technological task with our inverted gun arrangement. GPT and the theoretical predictions of Refs. [67,68] will be used in the design, optimization of the running conditions, and finally in the comparison with the data.

Declaration of competing interest

The authors declare that they have no known competing financial interests or personal relationships that could have appeared to influence the work reported in this paper.

Data availability

Data will be made available on request.

Acknowledgments

Appendix. Correlated and uncorrelated emittance calculations in GPT

GPT [42] defines the total normalized rms emittances for the $x–x'$ and $y–y'$ phase space as

$$\text{nemixrms} = \epsilon_{n,x,rms} = \gamma\beta\sqrt{\langle x_c^2\rangle \cdot \langle x_c'^2\rangle - \langle x_c x_c'\rangle^2} \text{ and}$$

$$\text{nemiyrms} = \epsilon_{n,y,rms} = \gamma\beta\sqrt{\langle y_c^2\rangle \cdot \langle y_c'^2\rangle - \langle y_c y_c'\rangle^2}.$$

where $x_c = x - \langle x\rangle$, $y_c = y - \langle y\rangle$, $x_c' = x' - \langle x'\rangle$, $y_c' = y' - \langle y'\rangle$. All parameters are centered around zero. The total emittance is then calculated by taking the geometric mean of "nemixrms" and "nemiyrms".

Further, GPT defines the normalized uncorrelated emittance as

$$\text{nemirrms} = \sqrt{\epsilon_{n,x,rms} \cdot \epsilon_{n,y,rms} - (\gamma\beta)^2 |\langle x_c y_c\rangle \cdot \langle x_c' y_c'\rangle - \langle x_c y_c'\rangle \cdot \langle x_c' y_c\rangle|}$$

where the second term is the normalized correlated emittance. The units of "nemixrms", "nemiyrms" and "nemirrms" are emittances in m-rad.

References

[1] A. Aprahamian, et al., Reaching for the horizon: The 2015 long range plan for nuclear science, 2015, https://inspirehep.net/literature/1398831.

[2] F. Willeke, The HERA lepton-proton collider, in: Challenges and Goals for Accelerator in the XXI Century, World Scientific, Singapore, 2016, http://dx.doi.org/10.1142/9789814436403_0015.

[3] M. Martini, Intra-beam scattering: Anatomy of the theory, in: Proc. CAS-CERN Accelerator School on Intensity Limitations in Particle Beams, Geneva, Switzerland, 2015, http://dx.doi.org/10.23730/CYRSP-2017-003.291.

[4] S. Nagaitsev, D. Broemmelsiek, A. Burov, K. Carlson, C. Gattuso, M. Hu, et al., Experimental demonstration of relativistic electron cooling, Phys. Rev. Lett. 96 (2006) 044801, http://dx.doi.org/10.1103/PhysRevLett.96.044801.

[5] M.W. Bruker, S. Benson, A. Hutton, K. Jordan, T. Powers, R. Rimmer, T. Satogata, A. Sy, H. Wang, S. Wang, H. Zhang, Y. Zhang, F. Ma, J. Li, X.M. Ma, L.J. Mao, X.P. Sha, M.T. Tang, J.C. Yang, X.D. Yang, H. Zhao, H.W. Zhao, Demonstration of electron cooling using a pulsed beam from an electrostatic electron cooler, Phys. Rev. Accel. Beams 24 (2021) 012801, http://dx.doi.org/10.1103/PhysRevAccelBeams.24.012801.

[6] A.V. Fedotov, et al., Experimental demonstration of hadron beam cooling using radio-frequency accelerated electron bunches, Phys. Rev. Lett. 124 (2020) 084801, http://dx.doi.org/10.1103/PhysRevLett.124.084801.

[7] Ya. Derbenev, Theory of electron cooling, 2017, http://dx.doi.org/10.48550/arXiv.1703.09735, arXiv.1703.09735.

[8] Ya. Derbenev, A. Skrinsky, Magnetization effect in electron cooling, Fiz. Plazmy 4 (1978) 492; Sov. J. Plasma Phys. 4 (1978) 273.

[9] D. Möhl, G. Petrucci, L. Thorndale, S. van der Meer, Physics and technique of stochastic cooling, Phys. Rep. 58 (1980) 73, http://dx.doi.org/10.1016/0370-1573(80)90140-4.

[10] S. van der Meer, Stochastic cooling and the accumulation of antiprotons, Rev. Modern Phys. 57 (1985) 689, http://dx.doi.org/10.1103/RevModPhys.57.689.

[11] J. Marriner, Stochastic cooling overview, Nucl. Instrum. Methods Phys. Res. A 532 (2004) 11–18, http://dx.doi.org/10.1016/j.nima.2004.06.025.

[12] W. Fischer, et al., RHIC performance with stochastic cooling for ions and head-on beam-beam compensation for protons, in: Proc. International Particle Accelerator Conference, Busan, Korea, 2016, http://dx.doi.org/10.18429/JACoW-IPAC2016-WEZA01.

[13] A.A. Mikhailichenko, M.S. Zolotorev, Optical stochastic cooling, Phys. Rev. Lett. 71 (1993) 4146–4149, http://dx.doi.org/10.1103/PhysRevLett.71.4146.

[14] J. Jarvis, V. Lebedev, A. Romanov, et al., Experimental demonstration of optical stochastic cooling, Nature 608 (2022) 287–292, http://dx.doi.org/10.1038/s41586-022-04969-7.

[15] V.N. Litvinenko, Ya.S. Derbenev, Coherent electron cooling, Phys. Rev. Lett. 102 (2009) 114801, http://dx.doi.org/10.1103/PhysRevLett.102.114801.

[16] V.N. Litvinenko, Y. Jing, D. Kayran, P. Inacker, J. Ma, T. Miller, I. Petrushina, I. Pinayev, K. Shih, G. Wang, Y.H. Wu, Plasma-cascade instability, Phys. Rev. Accel. Beams 24 (2021) 014402, http://dx.doi.org/10.1103/PhysRevAccelBeams.24.014402.

[17] G. Stupakov, P. Baxevanis, Microbunched electron cooling with amplification cascades, Phys. Rev. Accel. Beams 22 (2019) 034401, http://dx.doi.org/10.1103/PhysRevAccelBeams.22.034401.

[18] W.F. Bergan, P. Baxevanis, M. Blaskiewicz, E. Wang, G. Stupakov, Design of an MBEC cooler for the EIC, in: Proc. 12th International Particle Accelerator Conference, Campinas, SP, Brazil, 2021, http://dx.doi.org/10.18429/JACoW-IPAC2021-TUPAB179.

[19] Timothy J.P. Ellison, Electron cooling of high energy ion beams in RHIC and other facilities, Nucl. Instrum. Methods Phys. Res. A 364 (1995) 27–32, http://dx.doi.org/10.1016/0168-9002(95)00271-5.

[20] H. Zhao, J. Kewisch, M. Blaskiewicz, A. Fedotov, Ring-based electron cooler for high energy beam cooling, Phys. Rev. Accel. Beams 24 (2021) 043501, http://dx.doi.org/10.1103/PhysRevAccelBeams.24.043501.

[21] M. Blaskiewicz, Cooling of high-energy hadron beams, Annu. Rev. Nucl. Part. Sci. 64 (2014) 299, http://dx.doi.org/10.1146/annurev-nucl-102313-025427.

[22] G.I. Budker, An effective method of damping particle oscillations in proton and antiproton storage rings, Sov. At. Energy 22 (1967) 438, http://dx.doi.org/10.1007/BF01175204.

[23] G. Budker, N. Dikanskii, V. Kudelainen, I. Meshkov, V. Parkhomchuk, D. Pestrikov, A. Skrinskii, B. Sukhina, Experimental studies of electron cooling, Part. Accel. 7 (1976) 197–211, https://inspirehep.net/literature/116635.

[24] M.A. Al Mamun, P.A. Adderley, J.F. Benesch, B. Bullard, J.R. Delayen, J.M. Grames, J. Guo, F.E. Hannon, J.C. Hansknecht, C. Hernandez-Garcia, R. Kazimi, G.A. Krafft, M. Poelker, R.S. Suleiman, M.G. Tiefenback, Y. Wang, S. Zhang, S. Wijethunga, Production of magnetized electron beam from a DC high voltage photogun, in: Proc. 9th International Particle Accelerator Conference, Vancouver, BC, Canada, 2018, http://dx.doi.org/10.18429/JACoW-IPAC2018-THPMK108.

[25] M. Reiser, Theory and Design of Charged Particle Beams, Wiley-VCH, Weinheim, 2007.

[26] S.V. Benson, et al., Development of a bunched-beam electron cooler for the jefferson lab electron-ion collider, in: Proc. 9th Int. Particle Accelerator Conf. (IPAC'18), Vancouver, BC, Canada, 2018, http://dx.doi.org/10.18429/JACoW-IPAC2018-MOPMK015.

[27] D.H. Dowell, S.Z. Bethel, K.D. Friddell, Results from the average power laser experiment photocathode injector test, Nucl. Instrum. Methods Phys. Res. A 356 (1995) 167–176, http://dx.doi.org/10.1016/0168-9002(94)01327-6.

[28] D. Li, H. Feng, D. Filippetto, M. Johnson, A. Lambert, T. Luo, C. Mitchell, Ji Qiang, F. Sannibale, J. Staples, S. Virostek, R. Wells, Recent progress on the design of normal conducting APEX2 VHF CW electron gun, in: Proc. 10th International Particle Accelerator Conference, Melbourne, Australia, 2018, http://dx.doi.org/10.18429/JACoW-IPAC2019-TUPRB097.

[29] A. Romanov, C. Baffes, D. Broemmelsiek, D. Crawford, N. Eddy, Jr. Edstrom, E. Harms, J. Hurd, M. Kucera, J. Leibfritz, I. Rakhno, J. Reid, J. Ruan, J. Santucci, V. Shiltsev, G. Stancari, R. Thurman-Keup, A. Valishev, A. Warner, Commissioning and operation of FAST electron linac at Fermilab, in: Proc. 9th International Particle Accelerator Conference, Vancouver, BC, Canada, 2018, http://dx.doi.org/10.18429/JACoW-IPAC2018-THPMF024.

[30] A. Halavanau, P. Piot, D. Edstrom Jr., A. Romanov, Magnetized and flat beam generation at the Fermilab's FAST facility, in: Proc. 9th International Particle Accelerator Conference, Vancouver, BC, Canada, 2018, http://dx.doi.org/10.18429/JACoW-IPAC2018-THPAK061.

[31] Y.-E. Sun, P. Piot, K.-J. Kim, N. Barov, S. Lidia, J. Santucci, R. Tikhoplav, J. Wennerberg, Generation of angular-momentum-dominated electron beams from a photoinjector, Phys. Rev. ST Accel. Beams 7 (2004) 123501, http://dx.doi.org/10.1103/PhysRevSTAB.7.123501.

[32] A. Fetterman, D. Mihalcea, S. Benson, D. Crawford, D. Edstrom, F. Hannon, P. Piot, J. Ruan, S. Wang, Photoinjector generation of high-charge magnetized beams for electron-cooling applications, Nucl. Instrum. Methods Phys. Res. A 1025 (2022) 166051, http://dx.doi.org/10.1016/j.nima.2021.166051.

[33] I. Petrushina, V.N. Litvinenko, Y. Jing, J. Ma, I. Pinayev, K. Shih, G. Wang, Y.H. Wu, Z. Altinbas, J.C. Brutus, S. Belomestnykh, A. Di Lieto, P. Inacker, J. Jamilkowski, G. Mahler, M. Mapes, T. Miller, G. Narayan, M. Paniccia, T. Roser, F. Severino, J. Skaritka, L. Smart, K. Smith, V. Soria, Y. Than, J. Tuozzolo, E. Wang, B. Xiao, T. Xin, I. Ben-Zvi, C. Boulware, T. Grimm, K. Mihara, D. Kayran, T. Rao, High-brightness continuous-wave electron beams from superconducting radio-frequency photoemission gun, Phys. Rev. Lett. 124 (2020) 244801, http://dx.doi.org/10.1103/PhysRevLett.124.244801.

[34] W. Meissner, R. Ochsenfeld, Ein neuer effekt bei eintritt der supraleit-fähigkeit, Naturwissenschaften. 21 (1933) 787–788, http://dx.doi.org/10.1007/BF01504252.

[35] B.A. Knyazev, G.N. Kulipanov, N.A. Vinokurov, Novosibirsk terahertz free electron laser: instrumentation development and experimental achievements, Meas. Sci. Technol. 21 (2010) 054017, http://dx.doi.org/10.1088/0957-0233/21/5/054017.

[36] F. Ames, Y. Chao, K. Fong, S. Koscielniak, N. Khan, A. Laxdal, L. Merminga, T. Planche, S. Saminathan, D. Storey, C. Sinclair, The TRIUMF ARIEL RF modulated thermionic electron source, in: Proc. International Linear Accelerator Conference, East Lansing, MI, ISBN: 978-3-95450-169-4, 2016.

[37] Mark Stefani, Ph.D. thesis Old Dominion University, February 2021. http://dx.doi.org/10.25777/qx9c-ze88.

[38] W. Liu, S. Zhang, M. Stutzman, M. Poelker, Effects of ion bombardment on bulk GaAs photocathodes with different surface-cleavage planes, Phys. Rev. Accel. Beams 19 (2016) 103402, http://dx.doi.org/10.1103/PhysRevAccelBeams.19.103402.

[39] B. Dunham, J. Barley, A. Bartnik, I. Bazarov, L. Cultrera, J. Dobbins, G. Hoffstaetter, B. Johnson, R. Kaplan, S. Karkare, V. Kostroun, Y. Li, M. Liepe, X. Liu, F. Loehl, J. Maxson, P. Quigley, J. Reilly, D. Rice, D. Sabol, E. Smith, K. Smolenski, M. Tigner, V. Vesherevich, D. Widger, Z. Zhao, Record high-average current from a high brightness photoinjector, Appl. Phys. Lett. 102 (2013) 034105, http://dx.doi.org/10.1063/1.4789395.

[40] S. Benson, D. Douglas, G. Neil, M. Shinn, The Jefferson lab free electron laser program, J. Phys.: Conf. Ser. 299 (2011) 012014, http://dx.doi.org/10.1088/1742-6596/299/1/012014.

[41] X. Gu, Z. Altinbas, S. Badea, D. Bruno, L. Cannizzo, M. Costanzo, et al., Stable operation of a high-voltage high-current dc photoemission gun for the bunched beam electron cooler in RHIC, Phys. Rev. Accel. Beams 23 (2020) 013401, http://dx.doi.org/10.1103/PhysRevAccelBeams.23.013401.

[42] S. Van Der Geer, M. de Loos, General Particle Tracer (GPT). https://www.pulsar.nl/gpt/.

[43] Y. Wang, M.A. Mamun, P. Adderley, B. Bullard, J. Grames, J. Hansknecht, et al., Thermal emittance and lifetime of alkali-antimonide photocathodes grown on GaAs and molybdenum substrates evaluated in a -300 kV DC photogun, Phys. Rev. Accel. Beams 23 (2020) 103401, http://dx.doi.org/10.1103/PhysRevAccelBeams.23.103401.

[44] R.R. Mammei, R. Suleiman, J. Feingold, P.A. Adderley, J. Clark, S. Covert, et al., Charge lifetime measurements at high average current using a K_2 CsSb photocathode inside a DC high voltage photogun, Phys. Rev. ST Accel. Beams 16 (2013) 033401, http://dx.doi.org/10.1103/PhysRevSTAB.16.033401.

[45] M.A. Mamun, A. Elmustafa, M. Stutzman, P. Adderley, M. Poelker, Effect of heat treatments and coatings on the outgassing rate of stainless-steel chambers, J. Vac. Sci. Technol. 32 (2014) 021604, http://dx.doi.org/10.1116/1.4853795.

[46] C. Hernandez-Garcia, P. Adderley, B. Bullard, J. Benesch, J. Grames, J. Gubeli, et al., Compact -300 kV DC inverted insulator photogun with biased anode and alkali-antimonide photocathode, Phys. Rev. Accel. Beams 22 (2019) 113401, http://dx.doi.org/10.1103/PhysRevAccelBeams.22.113401.

[47] C. Hernandez-Garcia, D. Bullard, F. Hannon, Y. Wang, M. Poelker, High voltage performance of a DC photoemission electron gun with centrifugal barrel-polished electrodes, Rev. Sci. Inst. 88 (2017) 093303, http://dx.doi.org/10.1063/1.4994794.

[48] S.A.K. Wijethunga, M.A. Mamun, R. Suleiman, C. Hernandez-Garcia, B. Bullard, J.R. Delayen, J. Grames, G.A. Krafft, G. Palacios-Serrano, M. Poelker, Improving the electrostatic design of the jefferson lab 300 kV DC photogun, Rev. Sci. Instrum 93 (2022) 073303, http://dx.doi.org/10.1063/5.0091134.

[49] S. Zhang, et al., High current high charge magnetized and bunched electron beam from a dc photogun for JLEIC cooler, in: Proc. 10th International Particle Accelerator Conference, Melbourne, Australia, 2019, http://dx.doi.org/10.18429/JACoW-IPAC2019-TUPTS105.

[50] JLab TN 21-037 A Versatile and Highly Reliable Green-light Drive Laser for High Current Photoinjectors.

[51] Spiricon Laser Beam Diagnostics, https://www.ophiropt.com/user_files/laser/beam_profilers/lbausbuser.pdf.

[52] CST Studio Suite's, http://www.cst.com.

[53] Opera, https://www.3ds.com/products-services/simulia/products/opera.

[54] MATLAB, https://www.mathworks.com/products/matlab.html.

[55] S.A.K. Wijethunga, M.A. Mamun, F.E. Hannon, G.A. Krafft, J. Benesch, R. Suleiman, M. Poelker, J.R. Delayen, Simulation study of the magnetized electron beam, in: Proc. International Particle Accelerator Conference, Vancouver, Canada, 2018, http://dx.doi.org/10.18429/JACoW-IPAC2018-THPAK071.

[56] S.A.K. Wijethunga, Ph.D. thesis, Old Dominion University, 2021. http://dx.doi.org/10.25777/pgey-pd89.

[57] H. Wiedemann, Particle Accelerator Physics, fourth ed., Springer, Switzerland, 2015.

[58] H. Dowell, Sources of emittance in RF photocathode injectors: Intrinsic emittance, space charge forces due to non-uniformities, RF and solenoid effects, 2016, http://dx.doi.org/10.48550/arXiv.1610.01242, physics.acc-ph.

[59] L. Zheng, J. Shao, Y. Du, J.G. Power, E.E. Wisniewski, W. Liu, C.E. Whiteford, M. Conde, S. Doran, C. Jing, C. Tang, W. Gai, Overestimation of thermal emittance in solenoid scans due to coupled transverse motion, Phys. Rev. Accel. Beams 21 (2018) 122803, http://dx.doi.org/10.1103/PhysRevAccelBeams.21.122803.

[60] F. Hannon, M. Stefani, Transverse uncorrelated emittance diagnostic for magnetized electron beams, Phys. Rev. Accel. Beams 22 (2019) 102801, http://dx.doi.org/10.1103/PhysRevAccelBeams.22.102801.

[61] S. Full, A. Bartnik, I.V. Bazarov, J. Dobbins, B. Dunham, G.H. Hoffstaetter, Detection and clearing of trapped ions in the high current Cornell photoinjector, Phys. Rev. Accel. Beams 19 (2016) 034201, http://dx.doi.org/10.1103/PhysRevAccelBeams.19.034201.

[62] M.A. Mamun, M.R. Hernandez-Flores, E. Morales, C. Hernandez-Garcia, M. Poelker, Temperature dependence of alkali-antimonide photocathodes: Evaluation at cryogenic temperatures, Phys. Rev. Accel. Beams 20 (2017) 103403, http://dx.doi.org/10.1103/PhysRevAccelBeams.20.103403.

[63] M. Ferrario, M. Migliorati, L. Palumbo, Proceedings of the CAS-CERN Accelerator School, Geneva, 2014, http://dx.doi.org/10.5170/CERN-2014-009.331.

[64] I. Langmuir, The effect of space charge and residual gases on thermionic currents in high vacuum, Phys. Rev. 2 (1913) 450, http://dx.doi.org/10.1103/PhysRev.2.450.

[65] Y.Y. Lau, Simple theory for the two-dimensional Child-Langmuir law, Phys. Rev. Lett. 87 (2001) 278301, http://dx.doi.org/10.1103/PhysRevLett.87.278301.

[66] L.K. Ang, P. Zhang, Ultrashort-pulse Child-Langmuir law in the quantum and relativistic regimes, Phys. Rev. Lett. 98 (2007) 164802, http://dx.doi.org/10.1103/PhysRevLett.98.164802.

[67] D. Filippetto, P. Musumeci, M. Zolotorev, G. Stupakov, Maximum current density and beam brightness achievable by laser-driven electron sources, Phys. Rev. ST Accel. Beams 17 (2014) 024201, http://dx.doi.org/10.1103/PhysRevSTAB.17.024201.

[68] G. Shamuilov, A. Mak, K. Pepitone, V. Goryashko, Child-Langmuir law for photoinjectors, Appl. Phys. Lett. 113 (2018) 204103, http://dx.doi.org/10.1063/1.5063888.

[69] E. Wang, V.N. Litvinenko, I. Pinayev, M. Gaowei, J. Skaritka, S. Belomestnykh, I. Ben-Zvi, J.C. Brutus, Y. Jing, J. Biswas, J. Ma, G. Narayan, I. Petrushina, O. Rahman, T. Xin, T. Rao, F. Severino, K. Shih, K. Smith, G. Wang, Y. Wu, Long lifetime of bialkali photocathodes operating in high gradient superconducting radio frequency gun, Sci. Rep. 11 (2021) http://dx.doi.org/10.1038/s41598-021-83997-1.

[70] T. Maruyama, et al., A very high charge, high polarization gradient-doped strained GaAs photocathode, Nucl. Instrum. Methods Phys. Res. A 492 (2002) 199–211, http://dx.doi.org/10.1016/S0168-9002(02)01290-1.

[71] E. Wang, Ilan Ben-Zvi, Triveni Rao, D.A. Dimitrov, Xiangyun Chang, Qiong Wu, Tianmu Xin, Secondary-electron emission from hydrogen-terminated diamond: Experiments and model, Phys. Rev. Spec. Top. Accel. Beams 14 (2011) 111301, http://dx.doi.org/10.1103/PhysRevSTAB.14.111301.

[72] K. Togawa, et al., Surface charge limit in NEA superlattice photocathodes of polarized electron source, Nucl. Instrum. Methods Phys. Res. A 414 (1998) 431–445, http://dx.doi.org/10.1016/S0168-9002(98)00552-X.